COLLIDER PHENOMENOLOGY OF HEAVY NEUTRINOS

by

ARINDAM DAS

NOBUCHIKA OKADA, COMMITTEE CHAIR
BENJAMIN HARMS
PAOLO RUMERIO
PATRICK TOALE
RAINER SCHAD
KAUSTUBH AGASHE

A DISSERTATION

Submitted in partial fulfillment of the requirements
for the degree of Doctor of Philosophy
in the Department of Physics and Astronomy
in the Graduate School of
The University of Alabama

TUSCALOOSA, ALABAMA

2016

Abstract

The existence of the neutrino mass has been established by the neutrino oscillation experiments. The so-called seesaw extension of the Standard Model is probably the simplest idea to naturally explain the existence of tiny neutrino mass through the lepton number violating Majorana mass term. There is another alternative way, commonly known as the inverse seesaw mechanism, where the small neutrino mass is obtained by the tiny lepton number violating parameters.

In this work we investigate the signatures of such heavy neutrinos, having mass in the Electroweak scale at the high energy colliders. Based on a simple realization of inverse seesaw model we fix the model parameters to reproduce the neutrino oscillation data and to satisfy the other experimental constraints. We assume two flavor structures of the model and the different types of hierarchical light neutrino mass spectra. For completeness we consider the general parameterization for the model parameters by introducing an arbitrary orthogonal matrix and the nonzero Dirac and Majorana phases. Due to the smallness of the lepton number violating parameter this model can manifest the trilepton plus missing energy

at the Large Hadron Collider(LHC). Using the recent LHC results for anomalous production of the multilepton events at 8 TeV with a luminosity of 19.5 fb^{-1}, we derive the direct upper bounds on the light-heavy neutrino mixing parameter as a function of the heavy neutrino mass.

Using a variety of initial states such as quark-quark, quark-gluon and gluon-gluon as well as photon mediated processes for the Majorana heavy neutrinos we obtain direct upper bounds on the light-heavy neutrino mixing angles from the current LHC data at 8 TeV. For the pseudo-Dirac heavy neutrinos produced from the various initial states using the recent anomalous multilepton search by the LHC at 8 TeV with 19.5 fb^{-1} luminosity, we obtain the improved upper bounds on the mixing angles.

Dedication

Dedicated to the loving memory of my Dad

Thou hast made me endless, such is thy pleasure.
This frail vessel thou emptiest again and again,
and fillest it ever with fresh life.
This little flute of a reed thou hast carried over hills and dales, and hast breathed
through it melodies eternally new.
At the immortal touch of thy hands
my little heart loses its limits in joy and gives birth to utterance ineffable.
Thy infinite gifts come to me only on these very small hands of mine.
Ages pass, and still thou pourest, and still there is room to fill.

by
Rabindranath Tagore
(Song/ Poem Number 1 in Gitanjali (Song Offerings), Published by Macmillan And Co., Limited, St. Martin's Street, London, 1913)

List of Abbreviations and Symbols

SM	Standard Model
FND	Flavor Non-Diagonal
FD	Flavor Diagonal
CERN	Conseil Européen pour la Recherche Nucléaire
LHC	Large Hadron Collider
ILC	International Linear Collider
CMS	Compact Muon Solenoid
ATLAS	A Toroidal LHC ApparatuS
VBF	Vector Boson Fusion
CDF	Collider Detector at Fermilab
Dϕ	DZero/ D0
YM	Yang-Mills
EW	Electroweak
SSB	Spontaneous Symmetry Breaking
EWSB	Electroweak symmetry breaking

QED	Quantum Electrodynamics
H. c.	Hermitian conjugate
QCD	Quantum Chromodynamics
PMNS	Pontecorvo-Maki-Nakagawa-Sakata
VEV	Vacuum Expectation Value
CKM	Cabibbo-Kobayashi-Maskawa

Acknowledgements

I must convey my gratitude to my advisor Professor Nobuchika Okada for his continuous support in my voyage among the icebergs, in quest of knowledge. Without his endless encouragements and guidance I would not be able to find the touchstone of my thoughts in high energy physics.

I would like to thank my dissertation committee members Professor Benjamin Harms, Professor Paolo Rumerio, Professor Patrick Toale, Professor Rainer Schad from the Department of Physics and Astronomy, University of Alabama and Professor Kaustubh Agashe from the Maryland Center for Theoretical Physics (MCFP), Department of Physics, University of Maryland, College Park. I would like to thank all of my reference letter writers who devoted important time from their research to write letters for me. In this occasion I want to thank Professor Partha Konar, Professor Swapan Kumar Majhi, Professor Osamu Seto, Dr. Paratma Sri Bhupal Dev, Dr. Natsumi Nagata, Dr. Hieu Minh Tran, Dr. Satsuki Oda for their inspiring collaborations and useful discussions at different parts of the work. I want to thank American Physical Society (APS) and Indo-US Science and Technology Forum (IUSSTF) for supporting

my academic visit to Physical Research Laboratory (PRL), Ahmedabad, India in 2012 from USA. I would like to thank The University of Alabama at Tuscaloosa and the Department of Physics and Astronomy for the graduate supports, grants and fundings. I take this opportunity to express my deepest greetings to my friends and colleagues Dr. Joydeep Chakrabortty and Dr. Pradipta Ghosh for their discussions and helps at the time of my graduate days at UA. I want to give a warm thank you to my friends and mates at the Department of Physics and Astronomy, University of Alabama and especially to Andrea Chaney, Sergio Fabi, Shaoqi Hou, Lei Lu, Nathan Papapietro, Digesh Raut and Dai-suke Takahashi (Okinawa Institute of Science and Technology & Meijo University) for important discussions in physics and non physics issues.

I want to thank Professor Shibaji Banerjee, Professor Suparna Roy Chowdhury, Professor Sailendra Narayan Roy Choudhury from the Department of Physics, St. Xavier's College, Kolkata, India and Professor Dhruba Banerjee from the Department of Physics, Jadavpur University, Kolkata, India for useful discussions and helps not only in physics but beyond that. I would like to thank Professor Sarbari Guha from the Department of Physics, St. Xavier's College, Kolkata, India and Professor Debatosh Guha from the Institute of Radio Physics and Electronics, University of Calcutta, Kolkata for

their continuous support in my undergraduate days. Again in this occasion I would like to convey my emotional gratitude to all of those who came closer as friends and loved ones but left as strangers. At this moment I want to thank my school Ramakrishna Mission Boys' Home Schools, Rahara, West Bengal, India for giving me first light of knowledge which helped me to walk in the stormy nights of my life.

I would like to thank my family for giving me company at the time of sadness with unconditional love and endless support. Our sweetest songs are those of saddest thought. At last I would like to thank my wife Sangeeta for staying with me in my downs and crafting the waste land with beautiful acres of grass. A thing of beauty is always a joy for ever: its loveliness increases; it will never pass into nothingness.

Again, at the end I want to thank each and everyone of the University of Alabama, Tuscaloosa and specially the Department of Physics and Astronomy for presenting me the sweetest few years of my life and giving me my identity. Thank you all.

Contents

List of Figures

1 INTRODUCTION

Mother nature has crafted the whole universe with tiny fundamental building blocks. Each of the building blocks has its own properties. For a better visualization let us consider a brick. It is made up of a huge number of small entities called molecules and molecules are made of atoms. A single atom is made of electron(s) and a nucleus and a nucleus is a combination of proton(s) and neutron(s) generally. The proton and neutron are made up of quarks and gluons. To fit these building blocks into the universe four types of fundamental forces are introduced which could be read as the strong, electromagnetic, weak, and gravitational. There is a very important mathematical framework called the Standard Model which formulates the interactions between the fundamental building blocks through the interactions such as the strong, electromagnetic and weak in the quantum world. Gravity is still out of the box and it is an open challenge so far how to properly formulate the quantum picture of gravity. The SM has been proven to be highly successful and precise through lots of different experimental verifications in past and current decades.

The experiments at the Large Electron-Positron (LEP) collider at CERN have made precise measurements of the very important parameters of the SM, such as the weak mediator (W-boson and Z-boson) masses. The proton- antiproton collider known as the Tevatron at Fermilab (CDF and D0) measured the top quark mass. In the recent days the LHC at CERN has started playing an important role after detecting and measuring the Higgs boson mass.

Despite the amazing agreements between the theoretical predictions and experimental results regarding the SM there are still some open questions. One of them is the existence of the the neutrino mass. The recent neutrino oscillation experiments have proven the existence of neutrino mass and neutrino mixing. To include the neutrino mass we need to extend the SM with the introduction of some extra particles.

In this chapter we will briefly discuss the SM in Sec. 1.1, neutrino mass and oscillation in Sec. 1.2 and the possible simple extensions of the SM to explain the existence of the neutrino mass in Sec. 1.3.

1.1 Standard Model

The SM [11] [12] [13] obeys a chiral gauge theory which follows a non-Abelian Yang Mills (YM) theory [14] under the $SU(3)_c \otimes SU(2)_L \otimes U(1)_Y$ gauge group. The $SU(2)_L \otimes U(1)_Y$ is called the

	$\mathrm{SU}(3)_C$	$\mathrm{SU}(2)_L$	$\mathrm{U}(1)_Y$
q_L^i	**3**	**2**	$\frac{1}{6}$
u_R^i	**3**	**1**	$\frac{2}{3}$
d_R^i	**3**	**2**	$-\frac{1}{3}$
ℓ_L^i	**1**	**2**	$-\frac{1}{2}$
e_R^i	**1**	**1**	-1
H	**1**	**2**	$\frac{1}{2}$

Table 1.1. The particle contents of the SM. $i = 1, 2, 3$ is the generation index.

EW sector. After electroweak symmetry breaking (EWSB) the EW sector spontaneously breaks into $U(1)_{\mathrm{em}}$ through the vacuum expectation value (VEV) of a complex scalar, called the Higgs field. The $SU(3)_c$ sector remains unbroken. The particle content for the SM is given in Table 1.1, see [15] [16] [17] for detailed discussions on SM. In Table 1.1, q_L^i is the left handed quak doublet, u_R^i is the right handed up-type quark, d_R^j is the down-type right handed quark, ℓ_L^i is the lepton doublet, e_R^i is the right handed electron and H is the Higgs field where $i = 1, 2, 3$.

1.1.1 Kinetic term for the leptons

The fundamental interactions of the SM are mediated by the spin-1 gauge bosons. The interaction for the $U(1)_Y$ sector is mediated by a gauge boson B_μ from the corresponding hypercharge generator Y.

On the other hand $W_\mu = W_\mu^a T^a$ are the gauge bosons of the $SU(2)_L$ and the $SU(2)_L$ generators T^a satisfy the following Lie algerbra [18]

$$\left[T^a, T^b\right] = i\epsilon^{abc} T^c, \tag{1.1}$$

where $T^a = \frac{\sigma^a}{2}$ with σ^a as the Pauli matrices. The charge operator is given by the Gell-Mann-Okubo relation

$$Q = \frac{1}{2}\sigma^3 + Y \begin{pmatrix} 1 & 0 \\ \\ 0 & 1 \end{pmatrix}. \tag{1.2}$$

We can write the covariant derivative for the lepton doublet as as

$$\begin{aligned} \mathcal{D}_\mu^{\ell_L} &= \partial_\mu - i\frac{g}{2} \begin{pmatrix} 0 & \sqrt{2}W_\mu^+ \\ \\ \sqrt{2}W_\mu^- & 0 \end{pmatrix} - i\frac{g}{2} W_\mu^3 \begin{pmatrix} 1 & 0 \\ \\ 0 & -1 \end{pmatrix} - \\ & ig' Y_{\ell_L} B_\mu \end{aligned} \tag{1.3}$$

where g and g' are the $SU(2)_L$ and $U(1)_Y$ coupling constants, respectively and $W_\mu^\pm = \frac{W_\mu^1 \mp i W_\mu^2}{\sqrt{2}}$. The covariant derivative for the e_R is

$$\mathcal{D}_\mu^{e_R} = \partial_\mu - ig' Y_{e_R} B_\mu. \tag{1.4}$$

We can rotate the W_μ^3 and B_μ into physical gauge bosons using

$$\begin{pmatrix} W_\mu^3 \\ \\ B_\mu \end{pmatrix} = \begin{pmatrix} \cos\theta_w & \sin\theta_w \\ \\ -\sin\theta_w & \cos\theta_w \end{pmatrix} \begin{pmatrix} Z_\mu \\ \\ A_\mu \end{pmatrix}. \tag{1.5}$$

where θ_w is the weak mixing angle which can be defined as

$$\tan\theta_w = \frac{g'}{g}. \tag{1.6}$$

Using Eq. 1.5 we can write Eqs.(1.3) and (1.4) as

$$\mathcal{D}_\mu^{\ell_L} = \partial_\mu - i\frac{g}{2}\begin{pmatrix} 0 & \sqrt{2}W_\mu^+ \\ \\ \sqrt{2}W_\mu^- & 0 \end{pmatrix} - i\frac{g}{\cos\theta_w}(T^3 - Q_\ell \sin^2\theta_w)Z_\mu - ieQ_\ell A_\mu \tag{1.7}$$

and

$$\mathcal{D}_\mu^{e_R} = \partial_\mu - i\frac{g}{\cos\theta_w}(-Q_{\ell_R}\sin^2\theta_w)Z_\mu - ieQ_{eR}A_\mu, \tag{1.8}$$

respectively. Here e is the QED coupling constant, defined as $e = g\sin\theta_w$. Therefore the kinetic part of the Lagrangian of the lepton sector can be written as

$$\mathcal{L}_{kin}^{lepton} = \overline{\ell_L} i\gamma^\mu \mathcal{D}_\mu^{\ell_L}\ell_L + \overline{e_R} i\gamma^\mu \mathcal{D}_\mu^{e_R} e_R \tag{1.9}$$

where

$$\ell_L = \begin{pmatrix} \nu_L \\ \\ e_L \end{pmatrix}. \tag{1.10}$$

1.1.2 Electoweak symmetry breaking and Higgs mechanism

In the SM all of the particles and the $SU(2)$ gauge bosons are massless. The masses are generated through the spontaneous symmetry breaking (SSB) [19] [20] [21] [22] [23] of the EW symmetry. For this process the SM particle content includes the scalar particle H and the corresponding gauge invariant Lagrangian is

$$\mathcal{L}_{Higgs} = (\mathcal{D}_\mu^H H)^\dagger (\mathcal{D}^{H\mu}) - V(H^\dagger H), \tag{1.11}$$

where the scalar potential is

$$V(H^\dagger H) = \lambda \left(H^\dagger H - \frac{v^2}{2} \right)^2, \tag{1.12}$$

At the potential minimum, the Higgs field develops its VEV through the SSB as

$$< H >= \begin{pmatrix} 0 \\ \\ \frac{v}{\sqrt{2}} \end{pmatrix} \tag{1.13}$$

by which the EW symmetry is broken down, $SU(2)_L \otimes U(1)_Y \rightarrow U(1)_{\rm em}$. The covariant derivative in Eq.(1.11) is written as

$$\mathcal{D}_\mu^H = \partial_\mu - i\frac{g}{2} \begin{pmatrix} A_\mu^3 + \tan\theta_w B_\mu & \sqrt{2}W_\mu^+ \\ \\ \sqrt{2}W_\mu^- & -\frac{Z_\mu}{\cos\theta_w} \end{pmatrix}. \tag{1.14}$$

In EW symmetry breaking (EWSB) three out of four degrees of freedom of the Higgs doublet are eaten up by three linear combinations of the electroweak gauge bosons to form their longitudinal components while the fourth field corresponding to the unbroken $U(1)_{\rm em}$ symmetry remains massless. This is the photon (A) and it mediates the long range electromagnetic interaction. The three massive modes, such as W^+, W^- and Z mediate the short range weak interaction. The mass spectrum is given by

$$m_{W^\pm}^2 = \frac{1}{4}g^2v^2, \quad m_Z^2 = \frac{1}{4}\frac{g^2v^2}{\cos^2\theta_w}, \quad m_A^2 = 0. \tag{1.15}$$

After the three degrees of freedom are eaten up by the gauge fields, the remaining one is called the Higgs boson (h). In the unitary gauge the neutral component of H is expressed as

$$H(x) = \begin{pmatrix} 0 \\ \\ \frac{v+h(x)}{\sqrt{2}} \end{pmatrix}. \tag{1.16}$$

Using Eq. (1.16) we express the Higgs potential of Eq. (1.12) as

$$V = \lambda v^2 h^2 + \lambda v h^3 + \frac{\lambda}{4} h^4, \tag{1.17}$$

where the Higgs mass is $m_H = \sqrt{2\lambda v^2}$ and it has been recently measured by LHC at ATLAS [24], and CMS [25] as 125 GeV. The Higgs self coupling (λ) is still yet to be directly measured by any experiment. Theoretically we can calculate the value of λ as

$$\lambda = \frac{m_H^2}{2v^2} \sim 0.13 \tag{1.18}$$

with $v = 246$ GeV.

1.1.3 Yukawa interactions of the leptons

The Yukawa interaction for the lepton sector is given by

$$\mathcal{L}_{Yukawa}^{lepton} = Y_e \overline{\ell_L} H e_R + H.c., \tag{1.19}$$

and after the symmetry breaking the Dirac mass terms for the leptons are generated as

$$\mathcal{L}_{mass} = \frac{Y_e}{\sqrt{2}}(v+h)\Big[\overline{e_L}e_R + \overline{e_R}e_L\Big] \tag{1.20}$$

Using Eq. (1.20) we can define the fermion masses as [26]

$$\begin{aligned} m_e &= \frac{Y_e}{\sqrt{2}}v \sim 0.511 \quad \text{MeV}, \\ m_\mu &= \frac{Y_\mu}{\sqrt{2}}v \sim 105.666 \quad \text{MeV}, \\ m_\tau &= \frac{Y_\tau}{\sqrt{2}}v \sim 1.777 \quad \text{GeV}. \end{aligned} \tag{1.21}$$

Note that we can not write such mass term for the neutrinos in the SM because in the SM there is no right handed neutrino, and therefore the neutrinos were massless in the SM.

1.1.4 $SU(2)_L \otimes U(1)_Y$ gauge sector

For the gauge sector we can write the kinetic term as,

$$\mathcal{L}^{gauge}_{kinetic} = -\frac{1}{4}F^a_{\mu\nu}F^{a^{\mu\nu}} - \frac{1}{4}B_{\mu\nu}B^{\mu\nu} \tag{1.22}$$

where $F^a_{\mu\nu} = \partial_\mu A^a_\nu - \partial_\nu A^a_\mu + g\epsilon^{abc}A^b_\mu A^c_\nu$ and $B_{\mu\nu} = \partial_\mu B_\nu - \partial_\nu B_\mu$. Eq. (1.22) includes the 3-point interactions like $W^+W^-\gamma$, W^+W^-Z and the 4-point interactions like $W^+W^-\gamma\gamma$, W^+W^-ZZ, $W^+W^-\gamma Z$

and $W^+W^-W^+W^-$. The other interactions are prohibited by the $SU(2)_L \otimes U(1)_Y$ gauge symmetry.

1.1.5 Kinetic term for the quarks

Like the lepton sector in $SU(2)_L \otimes U(1)_Y$, the quark sector has 8 strong force carriers from the $SU(3)$ generators. These generators are denoted as λ^a $(a = 1 - 8)$, which satisfy the $SU(3)$ Lie algebra

$$[\lambda^a, \lambda^b] = if^{abc}\lambda^c \tag{1.23}$$

Here f^{abc} is the antisymmetric structure constant and the $SU(3)$ generators, λ^a, are called the Gell-Mann matrices [27] [28] [29]. The covariant derivative for the q_L is

$$\mathcal{D}_\mu^{\mu^{q_L}} = \partial_\mu - ig_s G_\mu - igW_\mu - iY_{q_L} B_\mu \tag{1.24}$$

where $G_\mu = G_\mu^a \lambda^a$ with G_μ^a is the gluon field. The covariant derivative for u_R is

$$\mathcal{D}_\mu^{u_R} = \partial_\mu - ig_s G_\mu - ig^{'} Y_{u_R} B_\mu, \tag{1.25}$$

and that for d_R is

$$\mathcal{D}_\mu^{d_R} = \partial_\mu - ig_s G_\mu - ig' Y_{d_R} B_\mu. \tag{1.26}$$

Therefore the Lagrangian quark kinetic term is given by

$$\mathcal{L}^{quark}_{kinetic} = \overline{q_L} i\gamma^\mu \mathcal{D}^{q_L}_\mu q_L + \overline{u_R} i\gamma^\mu \mathcal{D}^{u_R}_\mu u_R + \overline{d_R} i\gamma^\mu \mathcal{D}^{d_R}_\mu d_R. \quad (1.27)$$

1.1.6 $SU(3)$ gauge interaction

The gluon kinetic term in the $SU(3)$ theory can be written as

$$\mathcal{L}^{gluon}_{kinetic} = -\frac{1}{4} G^a_{\mu\nu} G^{a\mu\nu}, \quad (1.28)$$

where $G^a_{\mu\nu} = \partial_\mu G^a_\nu - \partial_\nu G^a_\mu + g_0 f^{abc} G^b_\mu G^c_\nu$, which includes 3-point and 4-point gluon-self interactions.

1.1.7 Yukawa interactions of quarks

The Yukawa interactions for the quarks are given by

$$\mathcal{L}_{Yukawa} = Y_u \overline{q_L} \tilde{H} u_R + Y_d \overline{q_L} H d_R + H.c. \quad (1.29)$$

from which the quark masses are generated after the symmetry breaking. $\tilde{H}$ is defined as $\tilde{H} = i\sigma_2 H^*$, so that

$$\langle \tilde{H} \rangle = i\sigma_2 \langle H^* \rangle = \begin{pmatrix} \frac{v+h}{\sqrt{2}} \\ 0 \end{pmatrix}. \quad (1.30)$$

and we get the Dirac mass terms for the quarks as

$$\mathcal{L}_{mass} = -m^u_{ij}\overline{u^i_L}u^j_R - m^d_{ij}\overline{d^i_L}d^j_R + H.c. \tag{1.31}$$

where

$$\begin{aligned} m^u_{ij} &= \frac{Y^u_{ij}}{\sqrt{2}}v, \\ m^d_{ij} &= \frac{Y^d_{ij}}{\sqrt{2}}v \end{aligned} \tag{1.32}$$

are the masses of the up and down sector quarks with m^u and m^d as 3×3 matrices. Diagonalizing m^u and m^d by a global unitary transformation from the so called flavor basis to the mass basis we can find the mass of the quarks. The neutral current between the quarks is given by

$$\begin{aligned} \mathcal{L}^q_{NC} &= -\frac{g}{\cos\theta_w}\Big[\begin{pmatrix}\overline{u^i_L} & \overline{d^i_L}\end{pmatrix}\gamma^\mu(T^3 - Q_{q_L}\sin^2\theta_w)\begin{pmatrix}u^i_L \\ \\ d^i_L\end{pmatrix} \\ &+ \frac{g}{\cos\theta_w}\overline{u^i_R}\gamma^\mu(-Q_{u_R}\sin^2\theta_w)u^i_R \\ &+ \frac{g}{\cos\theta_w}\overline{d^i_R}\gamma^\mu(-Q_{d_R}\sin^2\theta_w)d^i_R\Big]Z_\mu \end{aligned} \tag{1.33}$$

and the electromagnetic interaction is written as

$$\mathcal{L}^q_{\rm em} = -eQ_u\Big[\overline{u^i_L}\gamma^\mu u^i_L + \overline{u^i_R}\gamma^\mu u_{R^i}\Big]A^\mu - eQ_d\Big[\overline{d^i_L}\gamma^\mu d^i_L + \overline{d^i_R}\gamma^\mu d^i_R\Big]A^\mu \tag{1.34}$$

and we notice that Eqs. (1.33) and (1.34) are invariant under the flavor rotations and i is the generation index. For up (down) type quark $T^3 = \frac{1}{2}(-\frac{1}{2})$.

The charged current interaction between the quarks is written as

$$\mathcal{L}^q_{CC} = \frac{g}{\sqrt{2}}\Big[\overline{u_L}\gamma^\mu V_{CKM} d_L\Big]W^+_\mu + H.c., \tag{1.35}$$

where V_{CKM} in Eq. (1.35) is a unitary matrix known as the Cabbibo-Kobayashi- Maskawa matrix [30, 31]. For more than one generation case the flavor eigenstates for quarks are not the same as the mass eigenstates. The d-type quark mass eigenstate d' is connected to their flavor eigenstates d by the unitary transformation given by

$$\begin{pmatrix} d' \\ s' \\ b' \end{pmatrix} = V_{CKM} \begin{pmatrix} d \\ s \\ b \end{pmatrix}, \tag{1.36}$$

where

$$V_{CKM} = \begin{pmatrix} c_{12}c_{13} & s_{12}c_{13} & s_{13}e^{-i\delta} \\ -s_{12}c_{23} - c_{12}s_{23}s_{13}e^{i\delta} & c_{12}c_{23} - s_{12}s_{23}s_{13}e^{i\delta} & s_{23}c_{13} \\ s_{12}s_{23} - c_{12}c_{23}s_{13}e^{i\delta} & -c_{12}s_{23} - s_{12}c_{23}s_{13}e^{i\delta} & c_{23}c_{13} \end{pmatrix} \tag{1.37}$$

where $s_{ij} = \sin\theta_{ij}$, $c_{ij} = \cos\theta_{ij}$, δ is the Dirac CP-violating phase. The experimental value of the V_{CKM} is well measured and given as

$$V_{CKM} = \begin{pmatrix} 0.97428 \pm 0.00015 & 0.2253 \pm 0.0007 & 0.00347^{+0.00016}_{-0.00012} \\ 0.2252 \pm 0.0007 & 0.97345^{+0.00015}_{-0.00016} & 0.0410^{+0.0011}_{-0.0007} \\ 0.00862^{+0.00026}_{-0.00020} & 0.0403^{+0.0011}_{-0.0007} & 0.999152^{+0.000030}_{-0.000045} \end{pmatrix} \tag{1.38}$$

at the 95% C. L [26]. The quarks masses obtained experimentally are given as $m_u = 2.3$ MeV, $m_d = 4.8$ MeV, $m_s = 95$ MeV, $m_c = 1.275$ GeV, $m_b = 4.18$ GeV, $m_t = 173.21$ GeV in [26].

1.2 Neutrino mass and oscillation

Since neutrino mass generation will be discussed in detail in the following section, we may simply consider the neutrino mass term here. We consider two types of neutrino masses. One of them is the Dirac mass

$$\mathcal{L}_{\text{mass}} = m_\nu \overline{\nu_R} \nu_L + H.c. \tag{1.39}$$

and the other one is the Majorana mass,

$$\mathcal{L}_{\text{mass}} = m_\nu \overline{\nu_L^c} \nu_L + H.c. \tag{1.40}$$

The current experiments with the solar, atmospheric, reactor and accelerator neutrinos give very strong evidences of the neutrino flavor oscillations which was first investigated in Homesteak experiment[32] (and later in [33] [34] [35] [36] [37]). This tells us about the existence of the neutrino mass and the flavor mixing. The LEP analysis provides a very strong bound on the number of neutrino generations as $N_\nu = 2.980 \pm 0.0082 \sim 3$ [38, 39]. Using the flavor basis we can write the Charged Current (CC) interaction in the lepton sector in the flavor basis as

$$\mathcal{L}_{CC} = \frac{g}{\sqrt{2}} \Sigma_{\alpha=e,\mu,\tau} \overline{e_{\alpha_L}} \gamma^{\mu} \nu_{\alpha_L} W_{\mu}^{-} + H.c. \tag{1.41}$$

The particles propagate as their mass eigenstates. The SM neutrinos are transformed from the flavor basis (ν_{α_L}) into the mass basis ($\tilde{\nu_{j_L}}$) as

$$\nu_{\alpha_L} = U_{\alpha j} \tilde{\nu_{j_L}} \tag{1.42}$$

where U is 3×3 unitarity matrix, commonly known as the neutrino mixing matrix as described by U_{PMNS} where PMNS stands for Pontecorvo-Maki-Nakagawa-sakata [40, 41]. U_{PMNS} is parameterized by three Euler angles and a phase along with two additional phases if the neutrinos are Majorana particles,

$$U_{PMNS} = \begin{pmatrix} c_{12}c_{13} & s_{12}c_{13} & s_{13}e^{-i\delta} \\ -s_{12}c_{23} - c_{12}s_{23}s_{13}e^{i\delta} & c_{12}c_{23} - s_{12}s_{23}s_{13}e^{i\delta} & s_{23}c_{13} \\ s_{12}s_{23} - c_{12}c_{23}s_{13}e^{i\delta} & -c_{12}s_{23} - s_{12}c_{23}s_{13}e^{i\delta} & c_{23}c_{13} \end{pmatrix} \times diag\Big(1, e^{i\rho}, e^{i\phi}\Big), \tag{1.43}$$

where $s_{ij} = \sin\theta_{ij}$, $c_{ij} = \cos\theta_{ij}$, δ is the Dirac CP-violating phase and ρ , ϕ are the Majorana CP-violating phases. Therefore, for the

Dirac neutrinos we have seven free parameters which includes three neutrino masses, three mixing angles and the Dirac CP-violating phase. For Majorana neutrinos we have additional two Majorana phases. Now using the unitary matrix one can transform Eq. 1.41 into the mass basis (or mass eigenstate) of the neutrinos as

$$\mathcal{L}_{CC}^{mass} = \frac{g}{\sqrt{2}}\Sigma_{\alpha=e,\mu,\tau}\Sigma_{j=1,2,3}\overline{e_{\alpha_L}}\gamma^{\mu}U_{\alpha j}\tilde{\nu_{j_L}}W_{\mu}^{-} + H.c. \tag{1.44}$$

We can write the time evolution of the neutrinos in the flavor basis

$$i\frac{\partial\nu^{\alpha}}{\partial t} = (U^{\dagger}HU)_{\beta}^{\alpha}\nu^{\beta} \tag{1.45}$$

where H is the free Hamiltonian and according to relativistic theory $H \sim E(1 + \frac{m_j^2}{2E^2})$ and solving Eq. 1.45 we write

$$\nu(t)^j = e^{-iE(1+\frac{m_j^2}{2E^2})t}\nu(0)^j. \tag{1.46}$$

Now expressing the Eq. (1.46) into flavor basis for two flavors for simplicity using a 2-dimensional orthogonal matrix we can write,

$$\nu(t) = e^{-iE(1+\frac{m_2^2}{2E^2})t}\begin{pmatrix} \cos^2\theta e^{i\frac{\Delta m_{12}^2 t}{2E^2}} + \sin^2\theta & \sin\theta\cos\theta(e^{i\frac{\Delta m_{12}^2 t}{2E^2}} - 1) \\ \sin\theta\cos\theta(e^{i\frac{\Delta m_{12}^2 t}{2E^2}} - 1) & \sin^2\theta e^{i\frac{\Delta m_{12}^2 t}{2E^2}} + \cos^2\theta \end{pmatrix} \nu(0) \tag{1.47}$$

Where $\Delta m^2_{12} = m^2_1 - m^2_2$ with $j = 1, 2$. Therefore the probability of the flavor oscillation $\nu_e \to \nu_\mu$ transition from the (1, 2) element of Eq. (1.47) is given as

$$P(\nu_e \to \nu_\mu) = \sin^2 2\theta \sin^2(\frac{\Delta m^2_{12} t}{4E}). \tag{1.48}$$

From Eq. (1.48) we notice that the small neutrino mass difference between two flavors are responsible for the neutrino flavor oscillation. The existence of nonzero neutrino masses and flavor mixing has been established by various neutrino oscillation experiments [42]. The

Δm^2_{21}	$7.6 \times 10^{-5}\text{eV}^2$
$\lvert\Delta m_{31}\rvert^2$	$2.4 \times 10^{-3}\text{eV}^2$
$\sin^2 2\theta_{12}$	0.87
$\sin^2 2\theta_{23}$	0.999 from T2K[43]
$\sin^2 2\theta_{13}$	0.089 at Daya Bay [44]
	0.084 at Daya Bay 2015 Moriond [45]
	0.1 at RENO [46], [33]
	0.09 at Double Chooz [47]

Table 1.2. Central Value of neutrino oscillation data from different experiments

existing neutrino oscillation experiments can determine two mass squared differences of the neutrinos such as $\Delta m^2_{12} = m^2_2 - m^2_1$ and

$|\Delta m^3_{31}| = |m^2_1 - m^2_3|$ and $\sin^2 2\theta_{ij}$. These quantities are given in Table 1.2. For detailed discussions, see [33] [34] [35] [36] [37].

1.3 Models of Neutrino Mass

The existence of the tiny neutrino mass has been realized in many ways by the extensions of the SM. The simplest extensions of the SM are the seesaw and the inverse seesaw mechanisms where SM singlet right handed Majorana neutrinos are introduced to extend the SM. There are two other ways to generate the neutrino mass such as the type-II [48] and the type-III [49] seesaw mechanisms [1].

1.3.1 Seesaw mechanism

	$\mathrm{SU}(2)_L$	$\mathrm{U}(1)_Y$
ℓ^i_L	**2**	$-\frac{1}{2}$
N^β_R	**1**	0
e^i_R	**1**	-1
H	**2**	$\frac{1}{2}$

Table 1.3. The particle content of the type-I seesaw mechanism. $i = 1, 2, 3$ and $\beta = 1, 2, 3$ are the flavor indices.

The seesaw extension of the SM [50, 51] is probably the simplest idea for explaining the very small neutrino masses naturally, where

[1] In type-II seesaw we introduce $SU(2)_L$ thriplet scalar and in type-III we use $SU(2)_L$ triplet fermion to generate the Majorana mass term for the neutrinos.

the SM-singlet heavy right-handed Majorana neutrinos induce the dimension five operators, leading to very small light Majorana neutrino masses. The particle content for the seesaw extension of the SM is given in Tab. 1.3. In the so-called type-I seesaw [52, 53], we introduce SM gauge-singlet right handed Majorana neutrinos N_R^β. The relevant part of the Lagrangian is

$$\mathcal{L} \supset -Y_D^{\alpha\beta}\overline{\ell_L^\alpha}\tilde{H}N_R^\beta - \frac{1}{2}m_N^{\alpha\beta}\overline{N_R^{\alpha C}}N_R^\beta + H.c.. \tag{1.49}$$

After the spontaneous EWSB by the Higgs VEV we obtain the Dirac mass matrix as $M_D = \frac{Y_D v}{\sqrt{2}}$. Using the Dirac and Majorana mass matrices we can write the neutrino mass matrix as

$$M_\nu = \begin{pmatrix} 0 & M_D \\ M_D^T & m_N \end{pmatrix}. \tag{1.50}$$

Diagonalizing this matrix we obtain the seesaw formula for the light Majorana neutrinos as

$$m_\nu \simeq -M_D m_N^{-1} M_D^T. \tag{1.51}$$

The seesaw scale (the heavy neutrino mass scale) varies from the intermediate scale to the electroweak scale as we change the neutrino Dirac Yukawa coupling (Y_D) from the scale of top quark Yukawa

coupling ($Y_D \sim 1$) to the scale of electron Yukawa coupling ($Y_D \sim 10^{-6}$) to yield $m_\nu \sim 0.1$ eV.

In high energy collider experimental point of view, it is interesting if the heavy neutrino mass lies at the TeV scale or smaller, because such heavy neutrinos could be produced at high energy colliders, such as the LHC and the ILC being projected as energy frontier physics in the future. However, since the heavy neutrinos are singlet under the SM gauge group, they obtain the couplings with the weak gauge bosons only through the mixing via the Dirac Yukawa coupling. For the seesaw mechanism at the TeV scale or smaller, the Dirac Yukawa coupling is too small ($Y_D \lesssim 10^{-5}$) to produce the observable amount of the heavy neutrinos at the colliders. However, note that in the general parameterization for the seesaw formula [54] (see Chapter 4 for details), the Dirac Yukawa coupling can be sizable for the electroweak scale heavy neutrinos, while reproducing the neutrino oscillation data.

1.3.2 Inverse Seesaw Mechanism

There is another type of seesaw mechanism so-called the inverse seesaw [55], [56], where the small neutrino mass is obtained by tiny lepton-number-violating parameters, rather than the suppression by the heavy neutrino mass scale in the ordinary seesaw mechanism.

	SU(2)	$U(1)_Y$
ℓ	**2**	$-1/2$
H	**2**	$+1/2$
N_R	**1**	0
S_L	**1**	0

Table 1.4. Inverse seesaw extension of the SM

In the inverse seesaw scenario, the heavy neutrinos are pseudo-Dirac particles and their Dirac Yukawa couplings with the SM lepton doublets and the Higgs doublet can be even order one, while reproducing the small light neutrino masses. The particle content is given in Tab. 1.4. Thus, the heavy neutrinos in the inverse seesaw scenario can be produced at the high energy colliders through the sizable mixing with the SM neutrinos. The relevant part of the Lagrangian is given by [2]

$$\mathcal{L} \supset -Y_D^{\alpha\beta}\overline{\ell_L^\alpha}\tilde{H}N_R^\beta - m_N^{\alpha\beta}\overline{S_L^\alpha}N_R^\beta - \frac{1}{2}\mu_{\alpha\beta}\overline{S_L^\alpha}S_L^{\beta^C} + H.c., \quad (1.52)$$

where N_R^α and S_L^β are two SM-singlet heavy neutrinos with the same lepton numbers, m_N is the Dirac mass matrix, and μ is a small

[2] In order for inverse seesaw to work, it is crucial to forbid the Majorana mass term for N_R. For simple realization of the inverse seesaw mechanism in the next-to-minimal supersymmetryic SM, see [57]

Majorana mass matrix violating the lepton numbers. After the electroweak symmetry breaking we obtain the neutrino mass matrix as

$$M_\nu = \begin{pmatrix} 0 & M_D & 0 \\ M_D^T & 0 & m_N^T \\ 0 & m_N & \mu \end{pmatrix}. \tag{1.53}$$

Diagonalizing this mass matrix we obtain the light neutrino mass matrix

$$m_\nu \simeq M_D m_N^{-1} \mu m_N^{-1^T} M_D^T. \tag{1.54}$$

Note that the smallness of the light neutrino mass originates from the small lepton number violating term μ. The smallness of μ allows the $m_D m_N^{-1}$ parameter to be order one even for an electroweak scale heavy neutrino. Since the scale of μ is much smaller than the scale of m_N, the heavy neutrinos become the pseudo-Dirac particles. This is the main difference between the type-I and the inverse seesaws.

Through the seesaw mechanism, a flavor eigenstate (ν) of the SM neutrino is expressed in terms of the mass eigenstates of the light

(ν_m) and heavy (N_m) Majorana neutrinos such as[3]

$$\nu \simeq \mathcal{N}\nu_m + V_{\ell N} N_m, \tag{1.55}$$

where $V_{\ell N}$ is the mixing[4] between the SM neutrino and the SM-singlet heavy neutrino, and we have assumed a small mixing, $|V_{\ell N}| \ll 1$. Using the mass eigenstates, the charged current interaction for the heavy neutrino is given by

$$\mathcal{L}_{CC} = -\frac{g}{\sqrt{2}} W_\mu \bar{e} \gamma^\mu P_L \left(\mathcal{N}\nu_m + V_{\ell N} N_m\right) + H.c., \tag{1.56}$$

where e denotes the three generations of the charged leptons in the vector form, and $P_L = \frac{1}{2}(1-\gamma_5)$ is the projection operator. Similarly, the neutral current interaction is given by

$$\begin{aligned} \mathcal{L}_{NC} \;=\; & -\frac{g}{2c_w} Z_\mu \Big[\overline{\nu_m} \gamma^\mu P_L (V_{\ell N}^\dagger V_{\ell N}) \nu_m + \overline{N_m} \gamma^\mu P_L ({V_{\ell N}}^\dagger V_{\ell N}) N_m + \\ & \Big(\overline{\nu_m} \gamma^\mu P_L (\mathcal{N}^\dagger V_{\ell N}) N_m + H.c. \Big) \Big], \end{aligned} \tag{1.57}$$

where $c_w = \cos\theta_w$ with θ_w being the weak mixing angle. See, for example, [9] for the interaction Lagrangians and the partial decay widths of the heavy neutrinos.

[3]Except for the fact that the heavy neutrinos are Majorana particles, the following formulas are the same for type-I seesaw case.

[4]$V_{\ell N} = \mathcal{R} = \frac{m_D}{M}$

2 INVERSE SEESAW SIGNATURES AT LHC AND ILC

This chapter is organized as follows. In Sec. 2.1 we give the explicit formulas of the heavy neutrino production cross sections at the LHC and ILC and of the partial decay widths, which are used in our numerical analysis. In Sec. 2.2, we first fix the model parameters in simple parameterizations so as to satisfy the experimental constraints, assuming two flavor structures of our model and two types of hierarchical neutrino mass spectra. For completeness, we also consider a general parameterization of the neutrino Dirac mass matrix. In Sec 2.3, the signal of the heavy neutrinos at the LHC and ILC are investigated. For the general parameterization, we perform parameter scan to identify the parameter region that satisfies all experimental constraints, for which we examine how much the heavy neutrino signal is enhanced.

2.1 Productions and decays of heavy neutrinos at colliders

In the previous chapter, we have found the charged and neutral current interactions involving the heavy neutrinos. For detailed analysis, we need the information of the mixing matrices, $\mathcal{N}$ and $\mathcal{R}$. In the next section, we will fix all the elements of the matrices by considering the current experimental results. Before the analysis for fixing the parameters, in this section we give the formulas for the production cross sections and the partial decay widths of the heavy neutrinos in the limit of one generation and $\mathcal{N} = \mathcal{R} = 1$.

2.1.1 Production cross section at LHC

At the LHC, the heavy neutrinos can be produced through the charged current interactions by the s-channel exchange of the W boson. The main production process at the parton level is $u\bar{d} \to e^+ N_1$ (and $\bar{u}d \to e^- \overline{N_1}$) and the differential cross section is found to be

$$\begin{aligned} \frac{d\hat{\sigma}_{LHC}}{d\cos\theta} &= (3.89 \times 10^8 \text{ pb}) \times \frac{\beta}{32\pi\hat{s}} \frac{\hat{s}+M^2}{\hat{s}} \Big(\frac{1}{2}\Big)^2 3 \Big(\frac{1}{3}\Big)^2 \frac{g^4}{4} \\ &\quad \frac{(\hat{s}^2 - M^4)(2+\beta\cos^2\theta)}{(\hat{s}-m_W^2)^2 + m_W^2\Gamma_W^2}, \end{aligned} \tag{2.1}$$

where $\sqrt{\hat{s}}$ is the center-of-mass energy of the colliding partons, M is the mass of N_1, and $\beta = (\hat{s} - M^2)/(\hat{s} + M^2)$.

The total production cross section at the LHC is given by

$$\begin{aligned} \sigma_{LHC} &= \int d\sqrt{\hat{s}} \int d\cos\theta \int_{\hat{s}/E_{CMS}^2}^1 dx \frac{\sqrt{4\hat{s}}}{xE_{CMS}^2} f_u(x,Q) f_{\bar{d}} \left(\frac{\hat{s}}{xE_{CMS}}, Q \right) \frac{d\hat{\sigma}_{LHC}}{d\cos\theta} \\ &+ (u \to \bar{u}, \bar{d} \to d), \end{aligned} \tag{2.2}$$

where we have taken $E_{CMS} = 14$ TeV for the center-of-mass energy of the LHC. In our numerical analysis, we employ CTEQ5M [58] for the parton distribution functions for u-quark (f_u) and $\bar{d}$-quark ($f_{\bar{d}}$) with the factorization scale $Q = \sqrt{\hat{s}}$. The total cross section as a function of M is depicted in Fig. 2.1. Since we have fixed $\mathcal{N} = \mathcal{R} = 1$ in this analysis, the resultant cross section shown in Fig. 2.1 corresponds to the maximum values for a fixed M.

There are three main modes for the heavy neutrino decays: $N_1 \to e^- W^+, \nu_1 Z, \nu_1 h$. The corresponding partial decay widths are respectively given by

$$\begin{aligned} \Gamma(N_1 \to e^- W^+) &= \frac{g^2}{64\pi} \frac{(M^2 - m_W^2)^2 (M^2 + 2m_W^2)}{M^3 m_W^2}, \\ \Gamma(N_1 \to \nu_1 Z) &= \frac{g^2}{128\pi c_w^2} \frac{(M^2 - m_Z^2)^2 (M^2 + 2m_Z^2)}{M^3 m_Z^2}, \\ \Gamma(N_1 \to \nu_1 h) &= \frac{(M^2 - m_h^2)^2}{32\pi M} \left(\frac{1}{v \sin\beta} \right)^2. \end{aligned} \tag{2.3}$$

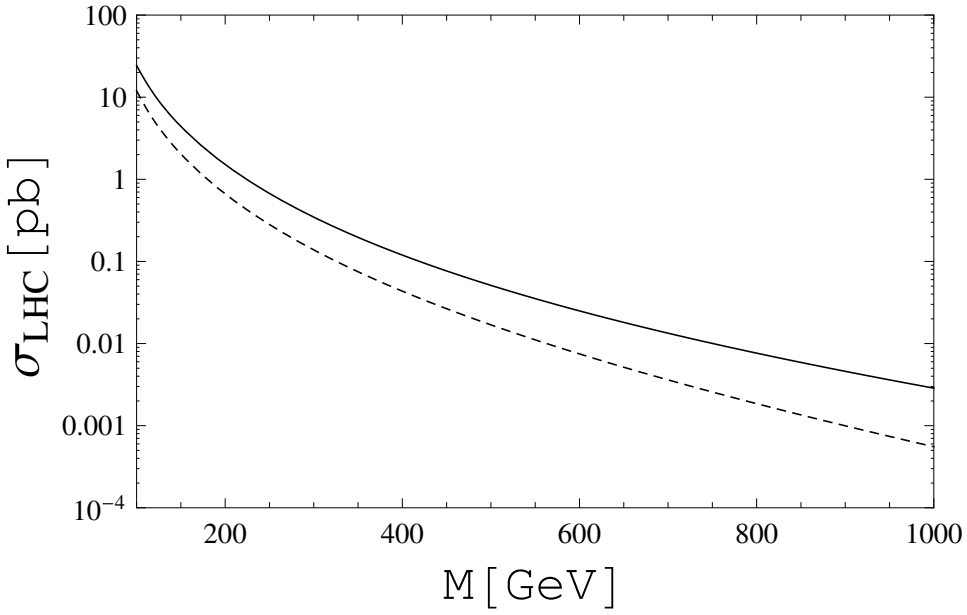

Fig. 2.1. The total production cross section of the heavy neutrino as a function of its mass at the LHC with $\sqrt{s} = 14$ TeV (solid line). As a reference, the production cross section at the LHC with $\sqrt{s} = 8$ TeV is also plotted (dashed line).

The long-sought Higgs boson was finally discovered by the ATLAS [24] and the CMS [25] collaborations at the LHC. According to the discovery, we use $m_h = 125.3$ GeV [25] in the following analysis. Our results are almost independent of the choice of the Higgs boson mass in the range of $125 - 126$ GeV.

2.1.2 Production cross section at ILC

The ILC can produce the heavy neutrino in the process $e^+e^- \to \overline{\nu_1}N_1$ through t and s-channels exchanging the W and Z bosons, respectively. The total differential production cross section for this

process is calculated as

$$
\begin{aligned}
\frac{d\sigma_{ILC}}{d\cos\theta} &= (3.89\times10^8 \text{ pb})\times\frac{\beta}{32\pi s}\frac{s+M^2}{s}\left(\frac{1}{2}\right)^2 \\
&\Big(\frac{16C_1^2C_2^2\left(s^2-M^4\right)(1+\cos\theta)(1+\beta\cos\theta)}{(M^2-\frac{s-M^2}{2}(1-\beta\cos\theta)-m_W^2)^2+m_W^2\Gamma_W^2} \\
&+ \frac{\left(4(C_{A_e}^2+C_{V_e}^2)(C_{A_\nu}^2+C_{V_\nu}^2)(1+\beta\cos^2\theta)\right)(s^2-M^4)}{(s-m_Z^2)^2+m_Z^2\Gamma_Z^2}+ \\
&\frac{(16C_{A_e}C_{V_e}C_{A_\nu}C_{V_\nu}(1+\beta)\cos\theta)\,(s^2-M^4)}{(s-m_Z^2)^2+m_Z^2\Gamma_Z^2} \\
&- 32C_1^2C_{A_e}^2(s^2-M^4)(1+\cos\theta)(1+\beta\cos\theta) \\
&\Big(\frac{\left(M^2-\frac{s-M^2}{2}(1-\beta\cos\theta)-m_W^2\right)(s-m_Z^2)}{((M^2-\frac{s-M^2}{2}(1-\beta\cos\theta)-m_W^2)^2+m_W^2\Gamma_W^2)((s-m_Z^2)^2+m_Z^2\Gamma_Z^2)} \\
&+ \frac{m_Wm_Z\Gamma_W\Gamma_Z}{((M^2-\frac{s-M^2}{2}(1-\beta\cos\theta)-m_W^2)^2+m_W^2\Gamma_W^2)((s-m_Z^2)^2+m_Z^2\Gamma_Z^2)}\Big) \\
&\Big), \qquad (2.4)
\end{aligned}
$$

where

$$\beta = (s-M^2)/(s+M^2), \qquad (2.5)$$

and

$$
\begin{aligned}
&C_1 = -C_2 = \frac{g}{2\sqrt{2}},\ C_{A_\nu} = C_{V_\nu} = \frac{g}{4\cos\theta_W}, \\
&C_{A_e} = \frac{g}{2\cos\theta_w}\left(-\frac{1}{2}+2\sin^2\theta_w\right),\ C_{V_e} = -\frac{g}{4\cos\theta_w}. \qquad (2.6)
\end{aligned}
$$

The total production cross section for the process $e^+e^- \to \overline{\nu_1}N_1$ for the ILC with $\sqrt{s} = 500$ GeV and 1 TeV, respectively, are shown in Fig. 2.2. Since we have fixed $\mathcal{N} = \mathcal{R} = 1$ in this analysis, the resultant cross section shown in Fig. 2.2 corresponds to the maximum values for a fixed M.

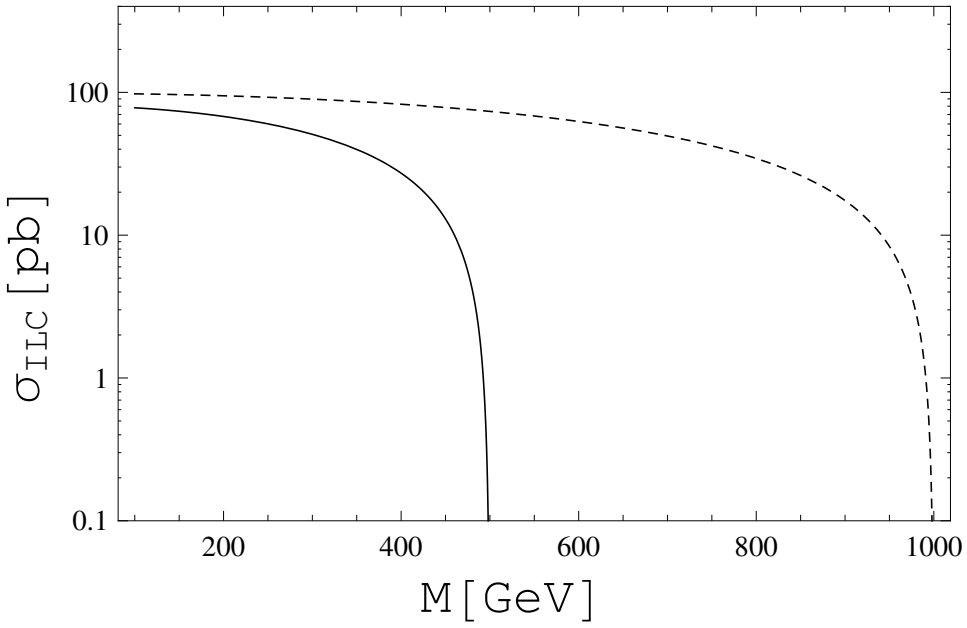

Fig. 2.2. The total production cross section of the process $e^+e^- \to \overline{\nu}_1 N_1$ at the ILC with $\sqrt{s} = 500$ GeV (solid line) and $\sqrt{s} = 1$ TeV (dashed line).

2.2 Fixing the matrices $\mathcal{N}$ and $\mathcal{R}$

2.2.1 Simple parameterizations

The elements of the matrices $\mathcal{N}$ and $\mathcal{R}$ are constrained by the experimental results [59], [60], [61], [62], [63]. We begin with the

current neutrino oscillation data. Recently non-zero reactor neutrino angle θ_{13} has been observed in several experiments, such as T2K [37], MINOS [35], Double CHOOZ [34], Daya Bay [36] and RENO [33], and their results are consistent with each other. Together with other oscillation data, all neutrino oscillation parameters except the Dirac CP-phase, two mass squared differences and three mixing angles have been measured in some precision. By using the data, we fix the neutrino mixing matrix elements. In the following analysis, we adopt $\sin^2 2\theta_{13} = 0.092$ [36] along with the other oscillation data: $\sin^2 2\theta_{12} = 0.87$, $\sin^2 2\theta_{23} = 1.0$, $\Delta m^2_{12} = m^2_2 - m^2_1 = 7.6 \times 10^{-5}$ eV^2, and $\Delta m^2_{23} = |m^2_3 - m^2_2| = 2.4 \times 10^{-3}$ eV^2. Then, the numerical values of neutrino mixing matrix elements are explicitly given by

$$U_{MNS} = \begin{pmatrix} 0.815 & 0.559 & 0.153 \\ -0.489 & 0.522 & 0.699 \\ 0.310 & -0.645 & 0.699 \end{pmatrix}, \tag{2.7}$$

where we have fixed all the CP-phases to be zero, for simplicity. We will discuss a general parameterization including all CP-phases as well as an arbitrary orthogonal matrix in the next subsection.

For the neutrino mass spectrum, we consider both the normal hierarchy (NH) and the inverted hierarchy (IH). The lightest mass

eigenstate is assumed to be very light and its mass is approximated as 0. Thus, in the NH case, the diagonal mass matrix is given by

$$D_{NH} = \mathrm{diag}\left(0, \sqrt{\Delta m^2_{12}}, \sqrt{\Delta m^2_{12} + \Delta m^2_{23}}\right), \tag{2.8}$$

while in the IH case

$$D_{IH} = \mathrm{diag}\left(\sqrt{\Delta m^2_{23} - \Delta m^2_{12}}, \sqrt{\Delta m^2_{23}}, 0\right). \tag{2.9}$$

In order to make our discussion simple, we assume the degeneracy of the heavy neutrinos in mass such as $m = M\mathbf{1}$ with the unit matrix $\mathbf{1}$, so that the neutrino mass matrix is simplified as

$$m_\nu = \mathcal{R}\mu\mathcal{R}^T = \frac{1}{M^2} m_D \mu m_D^T. \tag{2.10}$$

Moreover we consider two typical cases for the flavor structure of the model: (i) μ is also proportional to the unit matrix, $\mu \to \mu\mathbf{1}$. In this case, the flavor structure of m_ν is provided by a non-diagonal m_D. We call this case Flavor Non-Diagonal (FND) case. (ii) The other case is what we call Flavor Diagonal (FD) case, where m_D is proportional to the unit matrix, $m_D \to m_D\mathbf{1}$ and thus the flavor structure is encoded in the 3×3 matrix μ.

In the FND case, we consider two generations of N_j and N_j^c with $j = 1, 2$, so that

$$m_\nu = \frac{\mu}{M^2} m_D m_D^T = U_{MNS}^* D_{NH/IH} U_{MNS}^\dagger. \tag{2.11}$$

From this formula, we parameterize the neutrino Dirac mass matrix as

$$m_D = \frac{M}{\sqrt{\mu}} U_{MNS}^* \sqrt{D_{NH/IH}}, \tag{2.12}$$

where the matrices denoted as $\sqrt{D_{NH/IH}}$ are defined as

$$\sqrt{D_{NH}} = \begin{pmatrix} 0 & 0 \\ (\Delta m_{12}^2)^{\frac{1}{4}} & 0 \\ 0 & (\Delta m_{23}^2 + \Delta m_{12}^2)^{\frac{1}{4}} \end{pmatrix}, \tag{2.13}$$

and

$$\sqrt{D_{IH}} = \begin{pmatrix} (\Delta m_{23}^2 - \Delta m_{12}^2)^{\frac{1}{4}} & 0 \\ 0 & (\Delta m_{23}^2)^{\frac{1}{4}} \\ 0 & 0 \end{pmatrix}. \tag{2.14}$$

Note that in the case with two generations of N_j and N_j^c, the lightest mass eigenvalue is exactly 0. On the other hand, in the FD case, we have

$$m_\nu = \left(\frac{m_D}{M}\right)^2 \mu = U^*_{MNS} D_{NH/IH} U^\dagger_{MNS}. \tag{2.15}$$

Due to its non-unitarity, the elements of the mixing matrix $\mathcal{N}$ are severely constrained by the combined data from neutrino oscillation experiments, the precision measurement of weak boson decays, and the lepton-flavor-violating decays of charged leptons [59], [60], [61]. We update the results by using more recent data on the lepton-favor-violating decays [64], [65]:

$$|\mathcal{N}\mathcal{N}^\dagger| \;=\; \begin{pmatrix} 0.994 \pm 0.00625 & 1.499 \times 10^{-5} & 8.764 \times 10^{-3} \\ 1.499 \times 10^{-5} & 0.995 \pm 0.00625 & 1.046 \times 10^{-2} \\ 8.764 \times 10^{-3} & 1.046 \times 10^{-2} & 0.995 \pm 0.00625 \end{pmatrix} \tag{2.16}$$

Since $\mathcal{N}\mathcal{N}^\dagger \simeq \mathbf{1} - \epsilon$, we have the constraints on ϵ such that

$$|\epsilon| = \begin{pmatrix} 0.006 \pm 0.00625 & < 1.499 \times 10^{-5} & < 8.764 \times 10^{-3} \\ < 1.5 \times 10^{-5} & 0.005 \pm 0.00625 & < 1.046 \times 10^{-2} \\ < 8.76356 \times 10^{-3} & < 1.046 \times 10^{-2} & 0.005 \pm 0.00625 \end{pmatrix} \quad (2.17)$$

The most stringent bound is given by the $(1, 2)$ element which is from the constraint on the lepton-flavor-violating muon decay $\mu \to e\gamma$[1]. For the FND case, we describe ϵ as

$$\epsilon = \frac{1}{M^2} m_D m_D^T = \frac{1}{\mu} U_{MNS} D_{NH/IH} U_{MNS}^T, \quad (2.18)$$

and determine the minimum μ value (μ_{min}) so as to give $\epsilon_{12} = 1.5 \times 10^{-5}$ using the oscillation data in Eqs. (2.7), (2.8) and (2.9). We have found $\mu_{min} = 525$ eV and 329 eV for the NH and IH cases, respectively. Here we have used the fact that all parameters are real according to our assumption. In this way, we can completely determine the mixing matrix $\mathcal{R}$ and $\mathcal{N}$ from Eq. (2.12) by taking $\mu = \mu_{\rm min}$, which optimizes the production cross sections of the heavy

[1] It has been pointed out [66], [67] that in the SUSY inverse seesaw model, sparticle Z-penguin contributions can dominate the lepton-flavor-violating processes, independently of sparticle mass spectrum. According to the analysis in Ref. [67], we have found that the constraint from $\mu - e$ conversion process is more severe than the one from the $\mu \to e\gamma$ process for $M > 335$ GeV. Since we will focus on $M = 100 - 150$ GeV in the following analysis, we use the value of μ_{min} determined from the muon decay constraints.

neutrinos at the LHC and ILC. For the FD case, we simply take $\epsilon = (m_D/M)^2\mathbf{1} = 0.012251$ (95.5% CL).

2.2.2 General parameterization

For completeness, we also consider a general parameterization for the neutrino Dirac mass matrix for the FND case. From the inverse seesaw formula,

$$m_\nu = \mu\mathcal{R}\mathcal{R}^T = \frac{\mu}{M^2} m_D m_D^T = U^*_{MNS} D_{NH/IH} U^\dagger_{MNS}, \qquad (2.19)$$

we can generally parameterize $\mathcal{R}$ as

$$\mathcal{R}(\delta, \rho, x, y) = \frac{1}{\sqrt{\mu}} U^*_{MNS} \sqrt{D_{NH/IH}}\, O, \qquad (2.20)$$

where O is a general orthogonal matrix expressed as

$$O = \begin{pmatrix} \cos\alpha & \sin\alpha \\ -\sin\alpha & \cos\alpha \end{pmatrix} = \begin{pmatrix} \cosh y & i\sinh y \\ -i\sinh y & \cosh y \end{pmatrix} \begin{pmatrix} \cos x & \sin x \\ -\sin x & \cosh x \end{pmatrix}, \qquad (2.21)$$

with a complex number $\alpha = x + iy$, and the general form of the neutrino mixing matrix,

$$U_{MNS} = \begin{pmatrix} C_{12}C_{13} & S_{12}C_{13} & S_{13}e^{i\delta} \\ -S_{12}C_{23} - C_{12}S_{23}S_{13}e^{i\delta} & C_{12}C_{23} - S_{12}S_{23}S_{13}e^{i\delta} & S_{23}C_{13} \\ S_{12}S_{23} - C_{12}C_{23}S_{13}e^{i\delta} & -C_{12}S_{23} - S_{12}C_{23}S_{13}e^{i\delta} & C_{23}C_{13} \end{pmatrix} \times \begin{pmatrix} 1 & 0 & 0 \\ 0 & e^{i\rho} & 0 \\ 0 & 0 & 1 \end{pmatrix}. \quad (2.22)$$

Here, $C_{ij} = \cos\theta_{ij}$, $S_{ij} = sin\theta_{ij}$, δ is the Dirac phase and ρ is the Majorana phase. Thus, in this general parameterization, we have

$$\epsilon(\delta, \rho, y) = \mathcal{R}^*\mathcal{R}^T = \frac{1}{\mu} U_{MNS} \sqrt{D_{NH/IH}} O^* O^T \sqrt{D_{NH/IH}}^T U_{MNS}^\dagger \quad (2.23)$$

Note that

$$O^*O^T = \begin{pmatrix} \cosh^2 y + \sinh^2 y & -2i\cosh y \sinh y \\ 2i\cosh y \sinh y & \cosh^2 y + \sinh^2 y \end{pmatrix} \quad (2.24)$$

is independent of x, and hence the ϵ-matrix is a function of δ, ρ and y.

In the next section, we perform a parameter scan under the experimental constraints and identify an allowed region for the parameter set $\{\delta, \rho, y\}$. Then, we calculate the heavy neutrino production cross section for the parameter set and examine how much the production cross section is enhanced, satisfying the experimental constrains.

2.3 Collider signatures of heavy neutrinos

Let us now investigate the collider signatures of the heavy neutrinos with the information of $\mathcal{R}$ and $\mathcal{N}$ determined by the previous sections. In Sec. 1.3, we have already given the formulas used in our analysis in the limit of $\mathcal{R} = \mathcal{N} = 1$. It is easy to generalize the formulas with the concrete $\mathcal{R}$ and $\mathcal{N}$. The production cross section of the i-th generation heavy neutrino at the LHC, through the process $q\bar{q}' \to \ell N_i$ ($u\bar{d} \to \ell_\alpha^+ N_i$ and $\bar{u}d \to \ell_\alpha^- \overline{N_i}$) is given by

$$\sigma(q\bar{q}' \to \ell_\alpha N_i) = \sigma_{LHC} |\mathcal{R}_{\alpha i}|^2, \tag{2.25}$$

where σ_{LHC} is the cross section given in Eq. (2.2). Similarly, the production cross section at the ILC is

$$\sigma(e^+e^- \to \overline{\nu_\alpha} N_i) = \sigma_{ILC} |\mathcal{R}_{\alpha i}|^2, \tag{2.26}$$

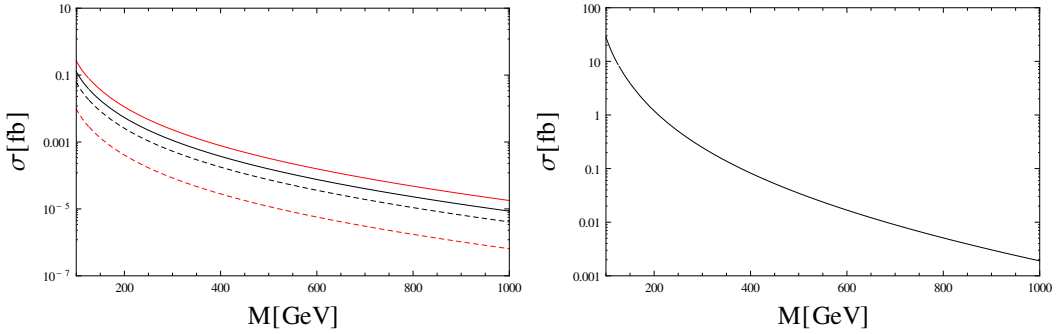

Fig. 2.3. Signal cross sections providing the tri-lepton final states for the FND (left panel) and FD (right panel) cases, at the LHC with $\sqrt{s} = 14$ TeV.

where σ_{ILC} is given in Eq. (2.4), and we have used the approximation $\mathcal{N}^\dagger\mathcal{R} \simeq U^\dagger_{MNS}\mathcal{R}$ because $|\epsilon_{\alpha\beta}| \ll 1$ as discussed in the previous section. The partial decay widths for the process $N_i \to \ell^-_\alpha W^+/\nu_\alpha Z/\nu_\alpha h$ are obtained by multiplying Eq. (2.3) and the factor $|\mathcal{R}_{\alpha i}|^2$ together.

2.3.1 Heavy neutrino signal at LHC with the simple parameterizations

As has been studied in Ref. [68] (see also [69] for the studies on the left-right symmetric model), the most promising signal of the heavy neutrino productions at the LHC is obtained by the final state with three charged leptons ($\ell^\pm\ell^\pm\ell^\mp$ with the total charge ±1) through the process $q\bar{q}' \to N\ell^\pm$ followed by $N \to \ell^\pm W^\mp$ and $W^\mp \to \ell^\mp\nu$. In this work, detailed studies have been performed for the signal of the heavy neutrino with a 100 GeV mass, which couples with either the electron or the muon. The events were pre-selected for two

like-sign charged leptons (ee or $\mu\mu$) to have transverse momentum $p_T > 30$ GeV. The decay mode, $N \to \nu Z$, followed by $Z \to \ell^+\ell^-$ is rejected by a cut for the invariant mass of the charge neutral dilepton. After elaborate selections, it has been concluded [70] that the heavy neutrino coupling to the muon could be observed at the LHC through the tri-lepton final states.

In our analysis, we follow the procedure in [68]. Since we are considering the general case with $\mathcal{R}$ and $\mathcal{N}$ consistent with the updated experimental data, the production cross sections of the heavy neutrinos are different from the ones in [68]. Fig. 2.3 shows the signal cross section providing tri-lepton final states with ee or $\mu\mu$ for the FND (left) and FD (right) cases, as a function of the heavy neutrino mass. In the left panel, the dashed and solid lines correspond to the NH and IH cases, respectively. The upper solid (dashed) line shows the cross sections with ee ($\mu\mu$).

We adopt the same efficiency for the signal events and the SM background events which was found in [68]. The number of events for tri-lepton final states with ee and $\mu\mu$, respectively, are listed on Table 2.1, for the luminosity 30 fb^{-1}. Unfortunately, the number of events for the FND case are found to be too small. This is because the component of $\mathcal{R}$ is severely constrained to be small by the current experiments. On the other hand, the FD case results the large

	ee	$\mu\mu$
FND (NH)	0.254	1.61
FND (IH)	7.00	3.38
FD	58.7	56.2
SM background	116.4	45.6

Table 2.1. Number of events at the LHC with $\sqrt{s} = 14$ TeV and 30 fb^{-1} luminosity, for the heavy neutrino mass $M = 100$ GeV.

number of signal events specially in the $\mu\mu$ case with a significance of more than 5-σ. If we naively estimate the significance by $S/\sqrt{B}$, the luminosity of 25 fb^{-1} (11 fb^{-1}) is required to achieve 5-σ significance for the ($\mu\mu$) final states.

2.3.2 Heavy neutrino signal at ILC with the simple parameterizations

The signature of heavy neutrinos at the ILC has been studied in detail based on the realistic Monte Carlo simulations in [71], [72]. In the studies, a five-dimensional model with bulk right-handed neutrinos [71] is considered and its 4-dimensional effective theory provides the Kaluza-Klein tower of the heavy neutrinos having sizable coupling to the weak gauge bosons through mixings with the SM light neutrinos. This structure of the couplings between the heavy neutrinos and the SM particles in the five-dimensional model is similar to the one in our inverse seesaw model. Thus, we apply the results

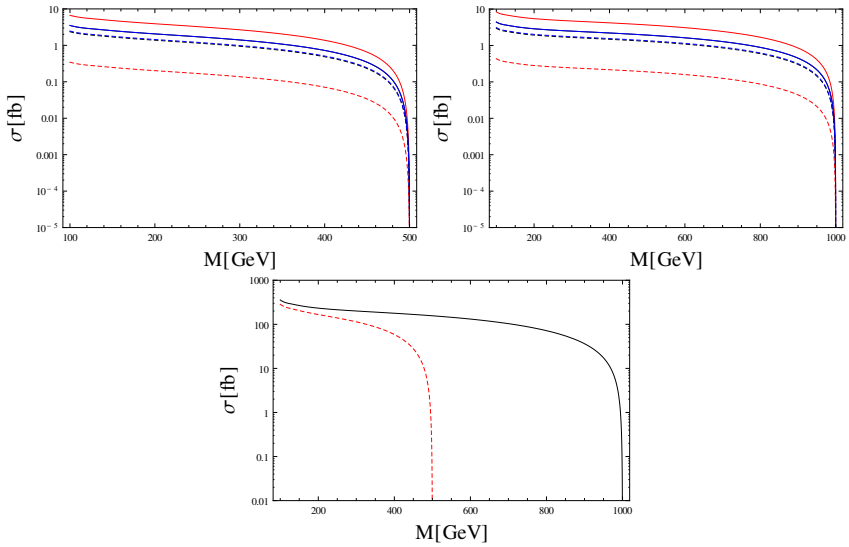

Fig. 2.4. The production cross sections for the process $e^+e^- \to \nu N$, followed by the decays $N \to \ell W$ ($\ell = e, \mu, \tau$) and $W \to q\bar{q}'$, as a function of the heavy neutrino mass. The upper-left panel shows the results for the FND case with $\sqrt{s} = 500$ GeV. The upper-right panel is the same as the upper-left panel but for the case with $\sqrt{s} = 1$ TeV. The results for the FD case are shown in the lower panel for $\sqrt{s} = 500$ GeV (solid) and $\sqrt{s} = 1$ TeV (dashed), respectively.

in [71], in particular, the signal and background selection procedure to our model.

According to [71], we focus on the two-jets and one isolated lepton signal with large missing energy at the ILC: $e^+e^- \to \nu N$, followed by the decays $N \to \ell W$ and $W \to q\bar{q}'$, through which the heavy neutrino production cross sections and the heavy neutrino mass can be reconstructed. The production cross sections for the process $e^+e^- \to \nu N$, followed by the decays $N \to \ell W$ ($\ell = e, \mu, \tau$) and $W \to q\bar{q}'$, as a function of the heavy neutrino mass are depicted in Fig. 2.4. The upper-left panel shows the results for the FND

case with $\sqrt{s} = 500$ GeV. The dashed lines from top to bottom denote the signal cross sections for $\ell = \tau$, μ and e, respectively, in the NH case. The two lines corresponding to $\ell = \tau$ and μ are well-overlapping. The solid lines from top to bottom denote the signal cross sections for $\ell = e$, τ and μ, respectively, in the IH case. The two dashed lines corresponding to $\ell = \mu$ and τ are well-overlapping. The upper-right panel is the same as the upper-left panel but for the case with $\sqrt{s} = 1$ TeV. The results for the FD case are shown in the lower panel for $\sqrt{s} = 500$ GeV (dashed) and $\sqrt{s} = 1$ TeV (solid), respectively. Here ℓ is either e, μ or τ.

For the ILC with $\sqrt{s} = 500$ GeV and the luminosity $\mathcal{L} = 500$ fb^{-1}, the signal and background events are listed on Table 2.2, Here, the final state of one electron and two jets with missing energy from anti-neutrinos is considered, and we have adopted the efficiencies found in [71], for $M = 150$ GeV. The main backgrounds are $e\nu W \to e\nu q\bar{q}$ and $WW \to \ell\nu q\bar{q}$, which are dramatically reduced by the selection using an isolated-electron track with a requirement of its energy range, 10 GeV$\leq E_e \leq$ 200 GeV, the requirement of the reconstructed di-jet mass to be consistent with W hypothesis etc (see [71] for details). The signal and background events for $\sqrt{s} = 1$ TeV and the same luminosity $\mathcal{L} = 500$ fb^{-1} are listed on Table 2.3. For completeness,

we have also listed the signal events (without cuts) for the case of $\ell = \mu$ and τ.

	Events before cuts	Events after cuts
FND (NH)	123.7	84.04
FND (IH)	2397	1363
FD	102210	69189.7
SM background	3210500	23346
FND (NH, $\ell = \mu$)	847.5	
FND (NH, $\ell = \tau$)	887.0	
FND (IH, $\ell = \mu$)	1261	
FND (IH, $\ell = \tau$)	1266	

Table 2.2. The number of events at the ILC with $\sqrt{s} = 500$ GeV and the luminosity 500 fb^{-1}, for the heavy neutrinos with mass 150 GeV. We have adopted the efficiencies for the signal and the SM background found by the realistic Monte Carlo simulations in [71].

In both $\sqrt{s} = 500$ GeV and 1 TeV, the signal to background ratio is large ($> 5 - \sigma$) for the FND (IH) and FD cases, while the significance is negligible for the FND (NH) case. If we naively expect a similar efficiency for the $\ell = \mu$ case, the heavy neutrinos can be observed with a large significance for both the FND and FD cases. In [71], the $\ell = \tau$ case is also analyzed in detail. In this case, the signal $N \to \nu e W(W \to q\bar{q}')$ is considered as the background, and the analysis depends on the number of the signal events and hence, we cannot simply adopt the results in [71]. However, since the main

	Events before cuts	Events after cuts
FND (NH)	162	52.0
FND (IH)	3133	776.1
FD	133605	42671.3
SM background	5476408	10500
FND (NH, $\ell = \mu$)	1108	
FND (NH, $\ell = \tau$)	1160	
FND (IH, $\ell = \mu$)	1648	
FND (IH, $\ell = \tau$)	1655	

Table 2.3. The same as Table 3, but $\sqrt{s} = 1$ TeV.

backgrounds are $e\nu W \to e\nu q\bar{q}$ and $WW \to \ell\nu q\bar{q}'$ also for this case, we can expect that the efficiency for our case is similar to the one obtained in [71], which is roughly the same as in the $\ell = e$ case. Thus, we expect, for the $\ell = \tau$ case, a large significance for the signal events in both the FND and the FD cases.

2.3.3 Heavy neutrino signal with the general parameterization

In the general parameterization for the FND case, $\mathcal{R}$ is a function of the Dirac phase (δ), the Majorana phase (ρ) and y in the general orthogonal matrix. In order to identify a region for these parameters satisfying the constraint on the ϵ-matrix, we perform a parameter scan by varying $-\pi \leq \delta, \rho \leq \pi$ with an interval of $\frac{\pi}{20}$ and $0 \leq y \leq 1$

with an interval of 0.02.[2] Then, for the identified parameters, we calculate the production cross section of the i-th generation heavy neutrino at the LHC through the process $q\bar{q}' \to \ell N_i$ ($u\bar{d} \to \ell_\alpha^+ N_i$ and $\bar{u}d \to \ell_\alpha^- \overline{N_i}$) given by

$$\sigma(q\bar{q}' \to \ell_\alpha N_i) = \sigma_{LHC} |\mathcal{R}_{\alpha i}(\delta, \rho, y)|^2, \tag{2.27}$$

where σ_{LHC} is the cross section given in Eq. (2.2). Similarly, the production cross section at the ILC is

$$\sigma(e^+e^- \to \overline{\nu_\alpha} N_i) = \sigma_{ILC} |\mathcal{R}_{\alpha i}(\delta, \rho, y)|^2, \tag{2.28}$$

where σ_{ILC} is given in Eq. (2.4), and we have used the approximation $\mathcal{N}^\dagger \mathcal{R} \simeq U_{MNS}^\dagger \mathcal{R}$ because $|\epsilon_{\alpha\beta}| \ll 1$ as discussed in the previous section. The partial decay widths for the process $N_i \to \ell_\alpha^- W^+ / \nu_\alpha Z / \nu_\alpha h$ are obtained by multiplying Eq. (2.3) and the factor $|\mathcal{R}_{\alpha i}(\delta, \rho, y)|^2$ together.

Fig. (2.5) shows the results of the parameter scan for the heavy neutrino production cross section with the tri-lepton final states at the LHC. Each dots satisfies the experimental constraints on all the ϵ-matrix elements. The first (second) column shows the results for the NH (IH) case. In the first (second) row, the results are shown as

[2] The Dirac mass matrix elements grow exponentially as we raise $|y|$. For a value $y > 1$, the neutrino oscillation data are realized under the fine-tuning between the large elements. Although the neutrino oscillation data are correctly reproduced for any values of y in the general parameterization, we only consider $y \leq 1$ to avoid the fine-tuning.

a function of δ (y) for the final state with two electrons, while the corresponding results for the final state with two muons are shown in the third and forth rows. Comparing the results with those for the simple parameterizations, the signal cross sections for the NH case receive significant enhancements for a certain parameter set, while for the IH case, we only have an enhancement by a factor $2 - 4$. The maximum signal cross sections we can achieve in the general parameterization are listed on Table 2.4. Interestingly, the maximum cross section for the NH case with the final state including two muons can even be larger than the one for the FD case.

Fig. 2.6 shows the cross section for the process $e^+e^- \to \nu N$, followed by the decays $N \to \ell W$ and $W \to q\bar{q}'$, at the ILC with $\sqrt{s} = 500$ GeV. Here we have fixed the heavy neutrino mass to be 150 GeV. Each dots satisfies the experimental constraints on all the ϵ-matrix elements. The first (second) column shows the results for the NH (IH) case. In the first (second) row, the results are shown

	ee	$\mu\mu$
NH (fb)	0.515	5.95
IH (fb)	0.575	0.475

Table 2.4. The maximum LHC cross sections for the final states with two electrons and two muons ,respectively, at the LHC with $\sqrt{s} = 14$ TeV.

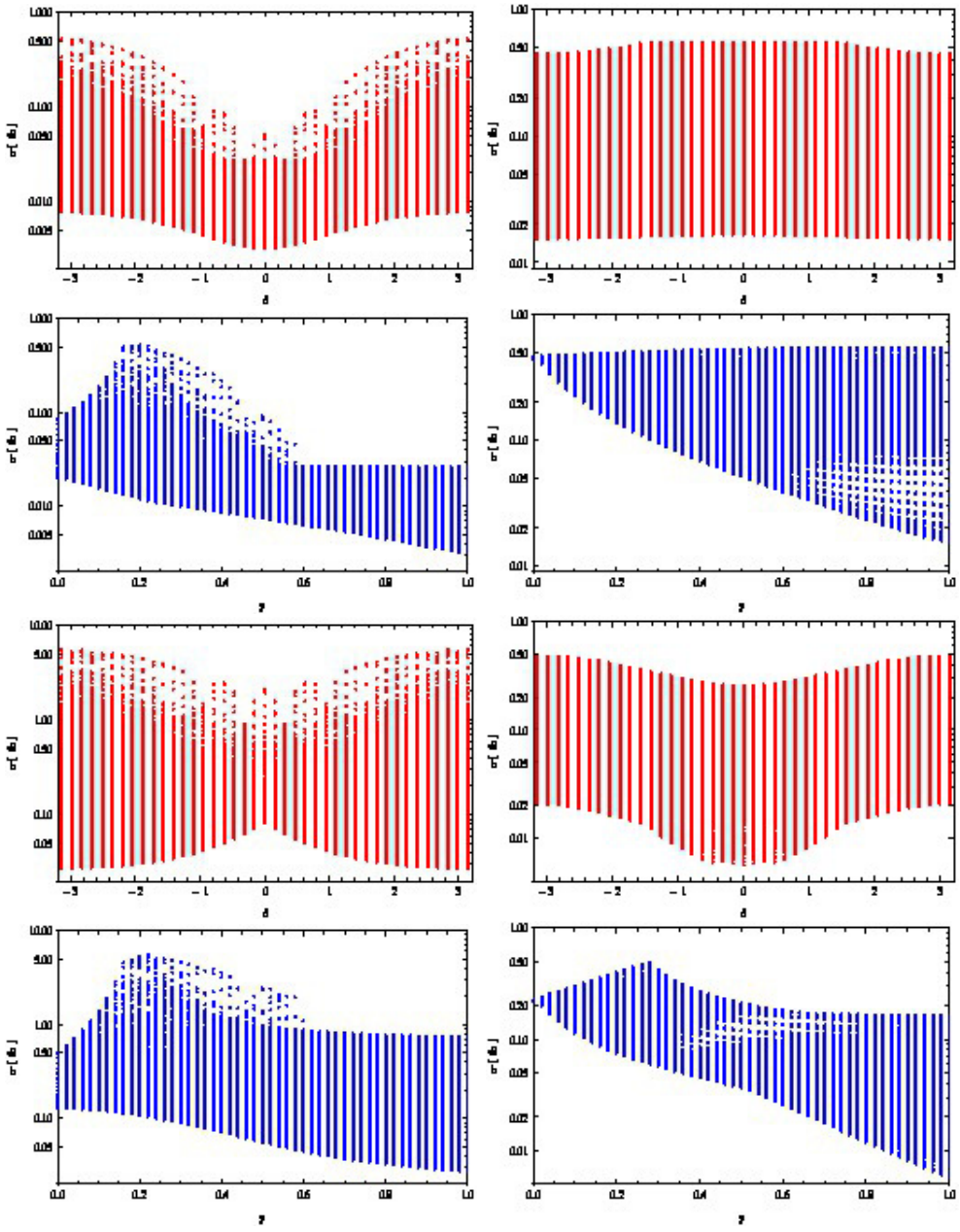

Fig. 2.5. Signal cross sections providing the tri-lepton final states as function of the Dirac phase (δ) and y for the heavy neutrino mass of 100 GeV, at the LHC with $\sqrt{s} = 14$ TeV. Each dot satisfies the experimental constraints on all the elements in the ϵ-matrix. The first (second) column corresponds to the results for the NH (IH) case. The first two rows are for the final states with two electrons, while the last tow are for the final states with two muons.

	NH (fb)	IH (fb)
$\ell = e$	8.5	8.5
$\ell = \mu$	130	11.0

Table 2.5. The maximum cross sections at the ILC with $\sqrt{s} = 500$ GeV. Here we have fixed the heavy neutrino mass to be 150 GeV. Each dots satisfies the experimental constraints on all the ϵ-matrix elements. The first (second) column shows the results for the NH (IH) case. The first and second rows correspond to the results for the case of $\ell = e$, while the corresponding results for the case of $\ell = \mu$ are shown in the third and forth rows.

	NH (fb)	IH (fb)
$\ell = e$	11.0	11.0
$\ell = \mu$	180	180

Table 2.6. The same as Table 2.5, but for $\sqrt{s} = 1$ TeV.

as a function of δ (y) for the case of $\ell = e$, while the corresponding results for the case of $\ell = \mu$ are shown in the third and forth rows. Similarly to the LHC results, we have found the significant enhancements for the NH case compared with the results for the simple parameterizations, while we have no significant enhancement for the IH case. The maximum signal cross sections we can achieve in the general parameterization are listed on Table 2.5. The maximum cross section for the NH case with $\ell = \mu$ can even be larger than the one for the FD case. We have performed the same analysis

also for the ILC with $\sqrt{s} = 1$ TeV. The maximum signal cross sections in this case are listed on Table 2.6. We have about a $30 - 40$ % enhancement in the cross sections by the increase of the collider energy.

The main backgrounds are $e\nu W \to e\nu q\bar{q}$ and $WW \to \ell\nu q\bar{q}$, which are dramatically reduced by the selection using an isolated-electron track with a requirement of its energy range, 10 GeV$\leq E_e \leq$ 200 GeV, the requirement of the reconstructed di-jet mass to be consistent with W hypothesis etc (see [71] for details). The maximum signal cross section for $\sqrt{s} = 1$ TeV and the same luminosity $\mathcal{L} = 500$ fb^{-1} are listed on Table 2.6. We have only listed e+jj and μ+jj signal cross section as functions of δ, ρ and y.

From Tables 2.5 and 2.6 the signal cross sections for μ+jj in NH dominates over IH by an order of magnitude for both the collider energies, $\sqrt{s} = 500$GeV and $\sqrt{s} = 1$ TeV. The signal cross sections for e+jj in NH is almost the same as that in the IH case for both the collider energies, $\sqrt{s} = 500$GeV and $\sqrt{s} = 1$ TeV. The $\mu\mu$ case cross sections at $\sqrt{s} = 500$GeV and $\sqrt{s} = 1$ TeV are some factors greater than the FD cases respectively.

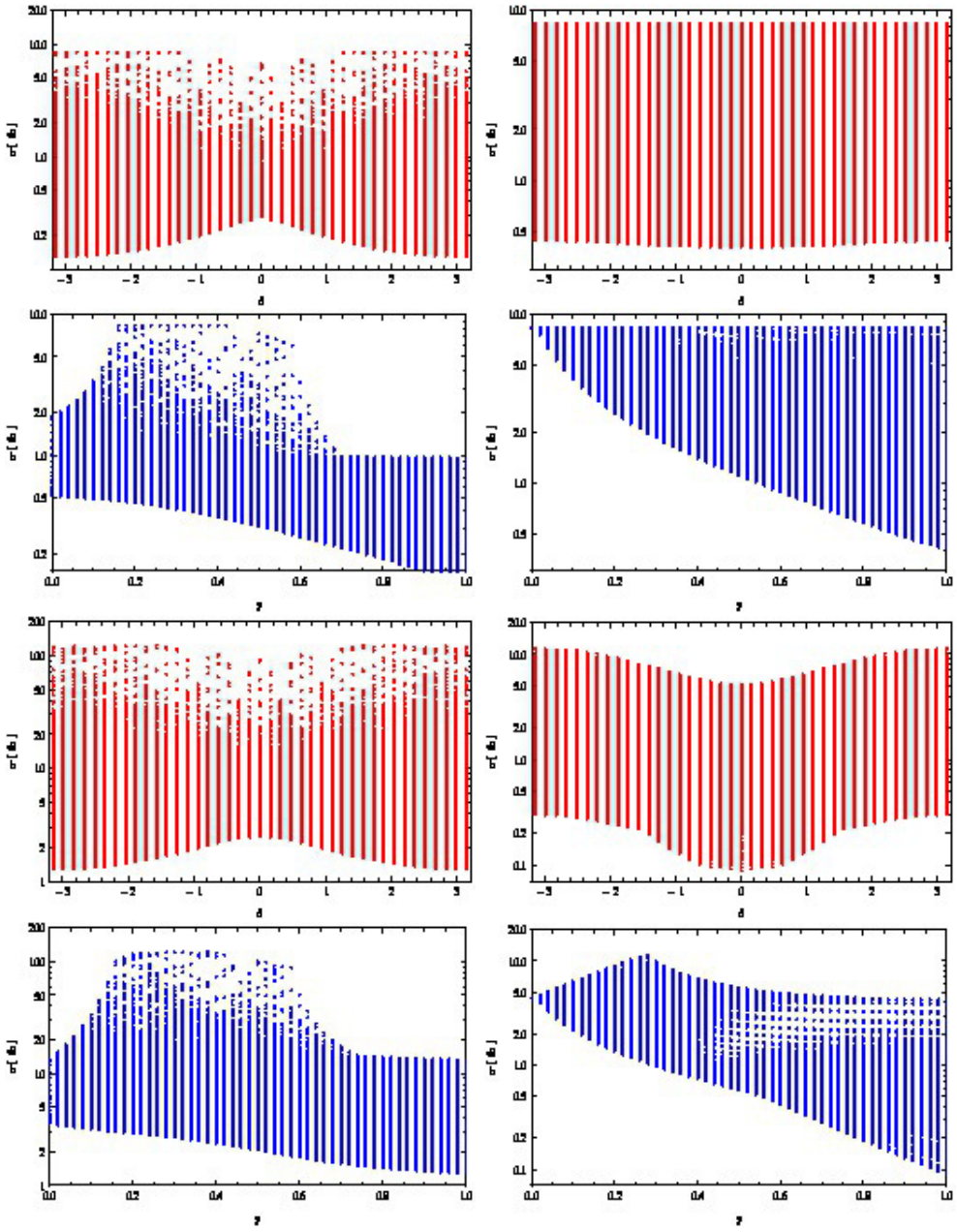

Fig. 2.6. The production cross sections for the process $e^+e^- \to \nu N$, followed by the decays $N \to \ell W$ ($\ell = e, \mu$) and $W \to q\bar{q}'$, as functions of the Dirac phase(δ) and y, at the ILC with $\sqrt{s} = 500$ GeV. Here we have fixed the heavy neutrino mass to be 150 GeV. Each dots satisfies the experimental constraints on all the ϵ-matrix elements. The first (second) column shows the results for the NH (IH) case. In the first (second) row, the results are shown as a function of δ (y) for the case of $\ell = e$, while the corresponding results for the case of $\ell = \mu$ are shown in the third and forth rows.

3 DIRECT UPPER BOUNDS ON ELECTROWEAK SCALE PSEUDO-DIRAC NEUTRINOS FROM $\sqrt{s} = 8$ TEV LHC DATA

The general feature of the inverse seesaw mechanism, i.e. a small lepton number breaking, allows large neutrino Yukawa couplings $Y_{l\alpha}$ up to $\mathcal{O}(1)$ even for an electroweak scale heavy neutrino mass M_N, without introducing any fine-tuning or cancellations in the light neutrino mass matrix. This leads to a number of interesting phenomenological consequences, such as large lepton flavor violation (LFV), non-unitarity of the leptonic mixing matrix [73], light DM candidate and modifications to the SM Higgs observables [57]. In this chapter, we will mostly focus on the collider signatures of this low-scale seesaw mechanism.

3.1 Trilepton Signature at the LHC

As far as the direct collider tests of the inverse seesaw mechanism are concerned, a large Yukawa coupling enhances the on-shell

production of electroweak-scale heavy neutrinos at the LHC. However, due to the small lepton number breaking in these scenarios, the heavy neutrinos are pseudo-Dirac, and hence, the 'smoking gun' collider signature of same-sign dilepton final states is suppressed. As the opposite-sign dilepton signal $l^{\pm}l^{\mp}jj$ is swamped with a large SM background, mainly from $pp \to Zjj$, the 'golden' channel for probing heavy Dirac neutrinos at the LHC is the trilepton final state:

$$\begin{aligned} pp &\to l_1^+ N \to l_1^+ l_2^- W^+ \to l_1^+ l_2^- l_3^+ \nu \,, \\ pp &\to l_1^- \bar{N} \to l_1^- l_2^+ W^- \to l_1^- l_2^+ l_3^- \bar{\nu} \,, \end{aligned} \tag{3.1}$$

as shown in Figure 3.1. Here N denotes a generic heavy neutrino mass eigenstate, which is typically the lightest SM-singlet fermion in a given seesaw model. From (1.53), we see that for $\|\mu\| \ll \|m_N\|$, the heavy neutrino masses given by the eigenvalues of M_ν can be approximated by degenerate pairs of the eigenvalues of $\begin{pmatrix} 0 & m_N^T \\ m_N & \mu \end{pmatrix}$. The small mass splitting between the quasi-Dirac pairs induced by the small lepton number breaking parameter μ is irrelevant for their collider studies, as long as μ is much smaller than their decay widths. This is a valid approximation in our case since we require relatively large neutrino Yukawa couplings in order to have a sizable collider

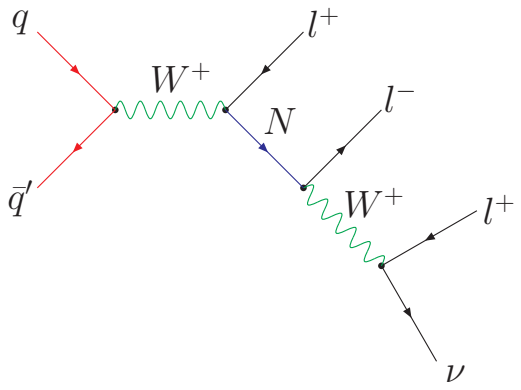

Fig. 3.1. The trilepton plus missing transverse energy signal of a heavy Dirac neutrino at the LHC.

signal and a very small μ to satisfy the neutrino oscillation data. Thus, we can treat the heavy neutrinos to be Dirac particles for our subsequent collider analysis. It is important to note here that the trilepton signal does not vanish in the $\mu \to 0$ limit. This is in contrast with the collider signature of heavy Majorana neutrinos in the minimal setup, where the same-sign dilepton signal must vanish in the limit of exact degeneracy.

The discovery potential of the trilepton channel (3.1) at the LHC, along with a detailed SM background analysis, was performed in [68] for a single-flavor electroweak-scale heavy neutrino. A more general heavy neutrino flavor structure was considered in [74], and it was shown that a 5σ statistical significance of the signal events over the SM background can be achieved at $\sqrt{s} = 14$ TeV LHC with 11 fb^{-1} luminosity in the flavor-diagonal case.

Meanwhile, the CMS collaboration has presented a model-independent search for anomalous production of events with at least three isolated charged leptons using the 19.5 fb^{-1} data at $\sqrt{s} = 8$ TeV LHC [1]. They have adopted a general search strategy which is applicable to a wide range of possible scenarios beyond the SM giving rise to a multilepton signal, including the pseudo-Dirac neutrino case discussed above. With this observation, we perform a collider simulation of the trilepton signal for a generic pseudo-Dirac heavy neutrino scenario with the same selection criteria as used in the CMS analysis, and compare our signal events with the CMS observed data. Using the fact that the experimental results are consistent with the SM expectations, we derive the first *direct* limits on the pseudo-Dirac heavy neutrino mass and mixing with the light neutrinos.

The inclusive cross section for the trilepton final state given by (3.1) in a generic seesaw model can be written as

$$\begin{aligned} \sigma(pp \to l_1 l_2 l_3 + \not{E}_T) &= \sigma_{\rm prod}(pp \to W^* \to N l_1) \\ &\quad \mathrm{BR}(N \to l_2 W)\, \mathrm{BR}(W \to l_3 \nu)\ . \end{aligned} \tag{3.2}$$

Here we assume that the heavy neutrinos are heavier than the W-boson so that the two-body decay $N \to lW$ is kinematically allowed, followed by an on-shell W-decay to SM leptons. In general, the final state charged leptons $l_{1,2,3}$ can be of any flavor combination.

However, since it is rather challenging to reconstruct the τ-lepton events with our simulation tools, we will only consider the electron and muon final states, i.e. $l = e, \mu$. In this case, the SM W branching ratio is given by $\mathrm{BR}(W \to l\nu) = 0.21$ [42], whereas the production cross section as well as the partial decay widths of the heavy neutrino depend on the light-heavy neutrino mixing parameter(s). The charge current and neutral current interactions are given in the preceding section.

3.2 Benchmark Scenarios

The flavor information of the final state leptons $l_1^{\pm} l_2^{\mp} l_3^{\pm}$ due to the production and decay of a particular heavy neutrino mass eigenstate N_i can be parametrized by $|\mathcal{R}_{l_1 i}\mathcal{R}_{l_2 i}|^2 / \sum_{l=e,\mu} |\mathcal{R}_{li}|^2$. For the collider simulation of our trilepton signal (3.1), we make some reasonable simplifying assumptions. The mixing matrix $\mathcal{R}$ can be approximated by $\mathcal{R} = M_D m_N^{-1}$. Furthermore, we assume flavor-diagonal Dirac mass matrices M_D and M_N, which suppress all LFV processes. This will always lead to a trilepton final state with opposite sign same flavor charged leptons (OSSF1 in the notation of [1]). Using the CMS observed number of events and the corresponding SM expectation values for the OSSF1 case [1], we will obtain direct constraints on the diagonal mixing elements of $\mathcal{R}$ in a model-independent way. Note

that the light neutrino oscillation data can still be satisfied with flavor-diagonal M_D and M_N by a suitable flavor structure of the lepton number breaking parameter μ; see [74] for an explicit numerical fit. For illustration, we will consider the following two benchmark cases with different relative magnitudes between the flavor Yukawa couplings:

(a) Single flavor (SF) case, in which one heavy Dirac pair is at the electroweak scale, while other heavy pairs are assumed to be beyond the kinematic reach of the LHC. With our flavor-diagonal choice, the lightest heavy Dirac neutrino mass eigenstates dominantly couple to a single lepton flavor l, which we assume to be muon for concreteness, although the same study equally applies for the electron-flavor case. Thus, we have the trilepton final states $l_1^{\pm} l_2^{\mp} l_3^{\pm}$ with both l_1 and l_2 of the muon flavor, while l_3 coming from the W-decay can be either electron or muon, i.e. our final state flavor compositions are $\mu^{\pm}\mu^{\mp}e^{\pm}$ and $\mu^{\pm}\mu^{\mp}\mu^{\pm}$. Note that in this case, the lightest heavy-neutrino branching fraction in (3.2) is independent of the mixing $\mathcal{R}_{\mu 1}$, and the only dependence on the mixing parameter appears in the production cross section, which is proportional to $|\mathcal{R}_{\mu 1}|^2$. Thus,

we can derive constraints on the single-flavor mixing parameter $|\mathcal{R}_{\mu 1}|^2 \equiv |B_{\mu N}|^2$, as a function of the lightest heavy Dirac neutrino mass m_N.

(b) Flavor diagonal (FD) case, in which two of the heavy Dirac neutrino pairs are degenerate with a common mass m_N. We further assume that one pair dominantly couples to electrons, and the other one to muons, but with equal strength, i.e., $|\mathcal{R}_{e1}| = |\mathcal{R}_{\mu 2}| \equiv |B_{lN}|$. Note that in the inverse seesaw with pseudo-Dirac neutrinos, the lepton number violating process of neutrinoless double beta decay ($0\nu\beta\beta$) is usually suppressed, and therefore, the stringent constraints on the active-sterile neutrino mixing in the electron sector (see e.g., [75]) may not apply. Hence, our benchmark case (b) with relatively large $|B_{eN}|^2$ is still allowed, except in special cases where the $0\nu\beta\beta$ amplitude could be enhanced [76]. In FD case, we have two additional final states $e^{\pm}e^{\mp}e^{\pm}$ and $e^{\pm}e^{\mp}\mu^{\mp}$, along with the two final states of the benchmark case (a). Thus the total trilepton signal cross section in case (b) is twice larger than that in case (a), and as a result, the limit on $|B_{lN}|^2$ derived in case (b) will be roughly twice stronger than the corresponding limit in case (a) for a given value of m_N.

3.3 Data Analysis and Results

For each of the above benchmark cases, the trilepton signal events were generated for $\sqrt{s} = 8$ TeV LHC by implementing the new charge current and neutral current interactions in `MadGraph5` [77]. The parton level cross sections were obtained using the `CTEQ6L` parton distribution functions [58]. The showering and hadronization of the events were performed with `PYTHIA6.4` [78] and a fast detector simulation was done using `DELPHES3`. Hadrons were clustered into jets using the anti-k_T algorithm as implemented in `FastJet2` [79] with a distance parameter of 0.5. In the detector simulation, we have considered the signal events containing three leptons accompanied by n-jets (with n = 1–4), after incorporating the MLM matching [80] prescription to avoid double counting of jets. For the generated signal events, we adopt the following basic selection criteria, as used in the CMS trilepton analysis [1]:

(i) The transverse momentum of each lepton: $p_T^l > 10$ GeV.

(ii) The transverse momentum of at least one lepton: $p_T^{l,\text{leading}} > 20$ GeV.

(iii) The jet transverse momentum: $p_T^j > 30$ GeV.

(iv) The pseudo-rapidity of leptons: $|\eta^l| < 2.4$ and of jets: $|\eta^j| < 2.5$.

(v) The lepton-lepton separation: $\Delta R_{ll} > 0.1$ and the lepton-jet separation: $\Delta R_{lj} > 0.3$.

(vi) The invariant mass of each OSSF lepton pair: $m_{l^+l^-} < 75$ GeV or > 105 GeV to avoid the on-Z region which was excluded from the CMS search. Events with $m_{l^+l^-} < 12$ GeV are rejected to eliminate background from low-mass Drell-Yan processes and hadronic decays.

(vii) The scalar sum of the jet transverse momenta: $H_T < 200$ GeV.

(viii) The missing transverse energy: $\not{E}_T < 50$ GeV.

Note that there are additional contributions to the trilepton signal from $N \to Z\nu, h\nu$, followed by Z, h decay to l^+l^-. However, the Z contributions are suppressed after we impose the m_{ll} cut to reduce the SM Z background, whereas the h contributions are additionally suppressed due to small Yukawa coupling of electrons and muons. The CMS analysis [1] has given the number of observed events and the corresponding SM background expectation for various ranges of $\not{E}_T$ and H_T that are sensitive to different kinematical and topological signatures. However, for our trilepton signal (3.1), the set of selection cuts listed above turn out to be the most efficient ones among those considered in the CMS analysis.

It is important to note here that in order to make a direct comparison of our signal events with the CMS results for the observed events and the SM background, we must include at least one jet with $p_T > 30$ GeV and $|\eta^j| < 2.5$ in the final state. The simplest trilepton final state shown in Figure 3.1 does not contain any jets at the parton-level, but initial state radiation (ISR) effects could give rise to final states with non-zero jets, though they are usually expected to be soft. However, there are additional diagrams involving quark-gluon fusion, such as those shown in Figure 3.2, which give rise to hard jets in the final state. The inclusive production cross section of the processes $pp \to Nl^+(\bar{N}l^-) + 1j$ is only a factor of 2–4 smaller than the original $pp \to Nl^+(\bar{N}l^-) + 0j$ process shown in Figure 3.1. This is due to the fact that, although the three-body final state Nlj is phase-space suppressed compared to the two-body final state Nl, there is a partially compensating enhancement at the LHC due to a much larger gluon content of the proton, as compared to the quark content [42]. The numerical values of the two production cross sections, normalized to $|B_{lN}|^2 = 1$, are shown in Figure 3.3 for both $\sqrt{s} = 8$ and 14 TeV LHC as a function of the lightest heavy neutrino mass m_N. Here we have shown the values for the SF case; for the FD case, the cross sections are enhanced by a factor of two. Note that for the $Nl + 1j$ case, we must use a non-zero p_T^j cut to avoid the

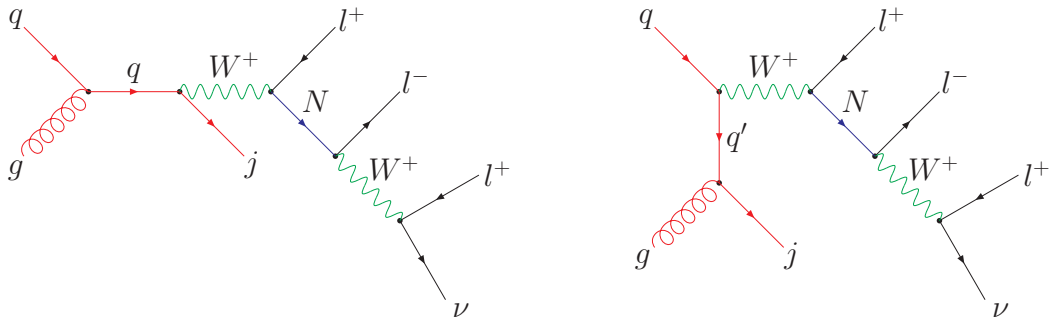

Fig. 3.2. The trilepton + one jet + missing transverse energy signal of a heavy Dirac neutrino at the LHC.

infrared singularity due to massless quarks in the t-channel. Here we have used the $p_T^j > 30$ GeV cut, following the CMS analysis, to get a finite result. Using a lower value of $p_T^{j,\min}$ could enhance the $Nl+1j$ cross section, thereby improving the signal sensitivity. A detailed detector-level simulation of these infrared-enhanced processes for different selection criteria than those used by the current CMS analysis is beyond the scope of this section, and will be presented in a separate communication. In this sense, the bounds on light-heavy neutrino mixing derived here can be treated as conservative bounds.

To derive the limits on $|B_{lN}|^2$, we calculate the normalized signal cross section $\sigma/|B_{lN}|^2$ at $\sqrt{s} = 8$ TeV LHC as a function of the lightest heavy neutrino mass m_N for both SF and FD cases, after imposing the CMS selection criteria listed above. The corresponding number of signal events passing all the cuts is then compared with

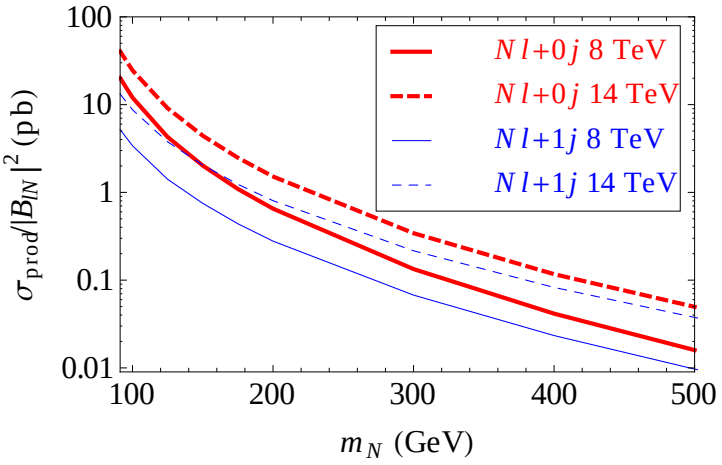

Fig. 3.3. The 'inclusive' parton-level cross sections for the processes $pp \to Nl^+ + \bar{N}l^-$ (thick, red) and $pp \to Nl^+j + \bar{N}l^-j$ (thin, blue) at $\sqrt{s} = 8$ TeV (solid) and 14 TeV (dashed) LHC. The results are shown for the single flavor (SF) case. For the flavor diagonal (FD) case, the numbers should be multiplied by a factor of two. For the Nlj case, we have imposed $p_T^j > 30$ GeV.

the observed number of events for 19.5 fb^{-1} luminosity [1]. For the selection criteria listed above, the CMS experiment observed (a) 510 events with the SM background expectation of 560 ± 87 events for $m_{l^+l^-} < 75$ GeV and (b) 178 events with the SM background expectation of 200 ± 35 events for $m_{l^+l^-} > 105$ GeV. Thus, for case (a), we have an upper limit of 37 signal events, and for case (b) an upper limit of 13 signal events. This sets a direct upper bound on the light-heavy neutrino mixing parameter $|B_{lN}|^2$ for a given value of m_N, as shown in Figure 3.4 for both cases (a) and (b) discussed above (thick dashed and solid lines, respectively). The case (b) becomes more efficient for higher values of m_N, thus setting a more stringent limit on $|B_{lN}|^2$. We have shown the 95% CL exclusion regions for

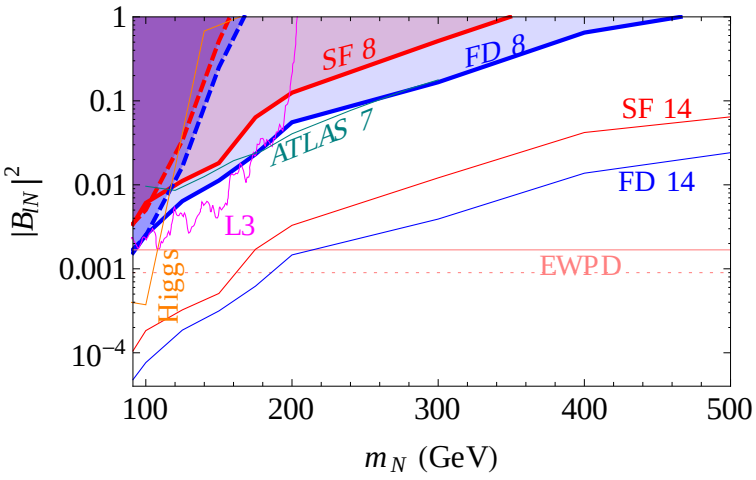

Fig. 3.4. The 95% CL upper limit on the light-heavy neutrino mixing parameter $|B_{lN}|^2$ as a function of the heavy Dirac neutrino mass m_N, derived from the CMS trilepton data at $\sqrt{s} = 8$ TeV LHC for 19.5 fb^{-1} luminosity [1]. The exclusion (shaded) regions are shown for two benchmark scenarios: (i) single flavor (SF) and (ii) flavor diagonal (FD), with two choices of the selection cut $m_{l^+l^-} < 75$ GeV (thick dotted) and > 105 GeV (thick solid). The corresponding conservative projected limits from $\sqrt{s} = 14$ TeV LHC data with 300 fb^{-1} integrated luminosity are shown by thin solid lines (SF 14 and FD 14). Some relevant existing upper limits (all at 95% CL) are also shown for comparison: (i) from a χ^2-fit to the LHC Higgs data [2] (Higgs), (ii) from a direct search at LEP [3] (L3), valid only for the electron flavor, (iii) ATLAS limit from $\sqrt{s} = 7$ TeV LHC data (ATLAS 7), valid for a heavy *Majorana* neutrino of the muon flavor, and (iv) indirect limit from a global fit to the electroweak precision data [4], [5], [6](EWPD), for both electron (solid) and muon (dotted) flavors.

both benchmark scenarios, namely SF and FD cases (red and blue shaded regions, respectively). As expected, the upper bound in the FD case is roughly twice as stronger than that in the SF case. In our analysis, we have considered heavy neutrino masses only above M_Z, since for $m_N < M_Z$, the existing LEP limits from Z-decay [81] are more stringent.

For comparison, we also show the 95% CL indirect upper limit on $|B_{lN}| < 0.030$ (0.041) for $l = \mu$ (e) derived from a global fit to the electroweak precision data [4], [5], (EWPD), which is independent of m_N for $m_N > M_Z$, as shown by the horizontal dotted (solid) line in Figure 3.4. We find that the direct bounds on $|B_{lN}|^2$ derived here are comparable to the indirect ones for $m_N \sim 100$ GeV, but get weaker at higher masses due to the suppression in the heavy neutrino production cross section (cf. Figure 3.3). Similar but somewhat weaker indirect bound could also be obtained from non-unitarity of the leptonic mixing matrix and lepton flavor universality constraints [59]. In addition, 95% CL constraints on the Yukawa coupling, and hence, on the mixing parameter $|B_{lN}|^2$ could be obtained from a χ^2-fit to the LHC Higgs data [2], as shown by the orange solid line (Higgs) in Figure 3.4. This limit turns out to be the strongest one for $m_N \lesssim M_h$, but becomes ineffective for larger m_N as N becomes off-shell in the Higgs decay $h \to N\nu \to 2l2\nu$.

Finally, we also compare the direct limits derived here with the existing collider bounds. The 95% CL LEP limit on $|B_{eN}|^2$, derived from the search channel $e^+e^- \to N_e\nu_e \to eW\nu_e$ [3], is shown by the pink solid line (L3) in Figure 3.4. For a small range of the parameter space, this limit is stronger than the LHC trilepton limit derived

here. However, the LEP limit is only applicable to the electron flavor, whereas the trilepton limit derived here is equally applicable to both electron and muon flavors. Moreover, the trilepton final states are also applicable to the heavy Majorana neutrino case, although the smoking gun collider signature in the Majorana case will be the same-sign dilepton final state, which is dominant over the trilepton signal. For completeness, we have shown the corresponding limits from a same-sign dimuon search by ATLAS using the $\sqrt{s} = 7$ TeV LHC data for 4.7 fb^{-1}. These limits are comparable to the trilepton limits derived here; however, a dedicated search optimized for the trilepton signal could lead to a more stringent limit than that presented here.

In light of the above results and the non-competitiveness of the direct bounds obtained here with the existing indirect limits, it might be useful to derive the projected direct limits anticipated from the $\sqrt{s} = 14$ TeV LHC data. Assuming that the signal efficiency is the same as that obtained for the $\sqrt{s} = 8$ TeV data analysis with $m_{l^+l^-} > 105$ GeV selection cut, and using the production cross sections given in Figure 3.3, we obtain the projected upper limits on $|B_{lN}|^2$ for both SF and FD cases at the $\sqrt{s} = 14$ TeV LHC with 300 fb^{-1} integrated luminosity, as shown by the thin solid red (SF 14) and blue (FD 14) lines in Figure 3.4. These limits should be treated as conservative

limits, since the signal-to-background selection efficiency at $\sqrt{s} = 14$ TeV LHC is expected to be *at least* as good as that in the $\sqrt{s} = 8$ TeV case. Thus, we find that the direct limits on the heavy-light neutrino mixing parameter are expected to improve significantly (by at least one order of magnitude) at the $\sqrt{s} = 14$ TeV LHC.

4 IMPROVED BOUNDS ON THE HEAVY NEUTRINO PRODUCTIONS AT THE LHC

In this chapter we study the heavy neutrino production at the LHC through a variety of initial states such as quark-quark $\left(q\overline{q'}\right)$, quark-gluon ($qg$) and gluon-gluon ($gg$) as well as the photon mediated processes. For fixed heavy neutrino masses (m_N) we calculate the individual cross sections of the respective processes normalized by the square of the mixing angles between light and the heavy neutrinos. We also study the kinematic distributions of the signal events produced by different initial states and find the characteristic distributions corresponding to the individual initial states.

For the Majorana heavy neutrino case we consider the same sign di-lepton plus two jet signal. Using the recent collider studies [82] [7] [8] we put an upper limit on the light-heavy mixing angles. For the pseudo-Dirac heavy neutrino we consider tri-lepton plus missing energy signal. We compare the upper bounds with those obtained by other experiments [83] [2] [3] [6] [4] [5]. Though some updated

analysis could be found in [84, 85] Using all the initial states the upper bounds given in [9] are improved.

This chapter is organized as follows. We calculate the production cross sections of the heavy neutrinos at the LHC with a variety of initial states in Sec 4.1. In Sec. 4.2 we simulate the signal events for the heavy neutrino productions. Comparing the generated events with the current LHC data, we obtain improved upper bounds on the mixing angles between the light-heavy neutrinos for the type-I and inverse seesaws, respectively.

4.1 Heavy neutrino production at the LHC

We implement our model in the generator `MadGraph5` [77] and calculate the production cross section of the heavy neutrino with a variety of initial states such as $q\overline{q'}$, qg and gg as well as photon mediated processes. For the final states we consider $N\ell + n-$jet, where the number of jets is $n = 0, 1, 2$. We separately calculate the production cross sections for individual initial states to understand which initial states dominantly contribute to the production process of the heavy neutrino.

4.1.1 $N\ell$ and $N\ell j$ production processes from $q\overline{q'}$ and qg initial states

We first consider the final state $N\ell$ from $q\overline{q'}$, and $N\ell j$ from both of $q\overline{q'}$ and qg initial states. The relevant Feynman diagrams with the initial $q\overline{q'}$ state are shown in Figs. 4.1 and 4.2, while those with the initial qg state are shown in Fig. 4.3. Fig. 4.4 shows the combined heavy neutrino production cross section normalized by the square of the mixing angle from the two initial states. For the final state $N\ell j$ we impose the minimum transverse momentum of the jet (p_T^j) as 10 GeV, 20 GeV and 30 GeV, respectively. In generating the events we set the `Xqcut`= p_T^j in MadGraph with the `MLM` matching scheme (`ickkw`= 1). The left panel shows the results for $\sqrt{s}$ =8 TeV, while $\sqrt{s}$ =14 TeV LHC results are shown in the right panel. The $N\ell j$ cross section dominates over the production, while for a higher p_T^j cut the $N\ell$ cross section dominates.

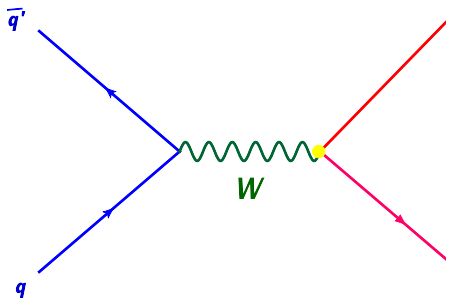

Fig. 4.1. Feynman diagram for $N\ell$ production from the $q\overline{q'}$ annihilation.

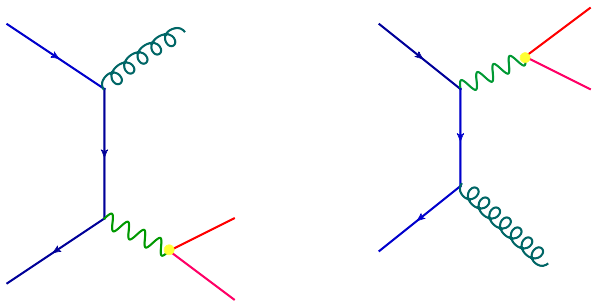

Fig. 4.2. Feynman diagrams for $N\ell j$ production from the $q\overline{q'}$ annihilation.

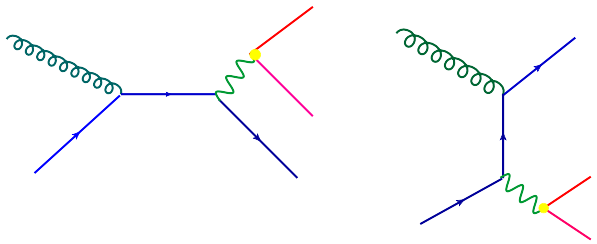

Fig. 4.3. Feynman diagrams for $N\ell j$ production from the qg fusion.

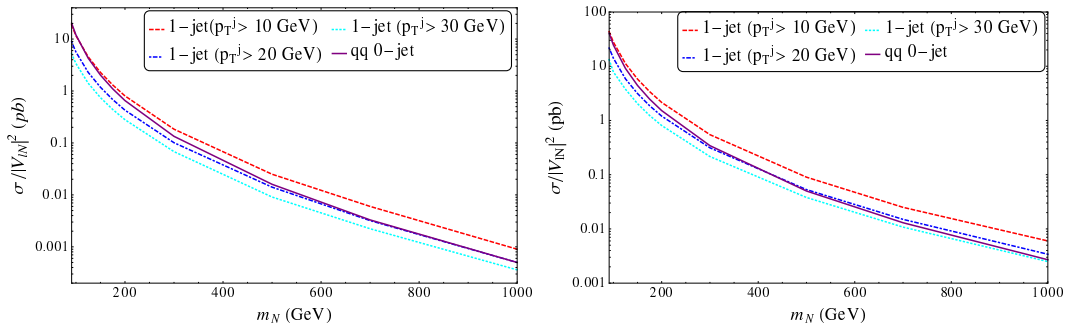

Fig. 4.4. The left panel shows the cross sections as a function of m_N normalized by the square of the mixing angle for the $N\ell j$ final state at the $p_T^j > 10$ GeV (dashed), $p_T^j >$20 GeV (dot-dashed) and $p_T^j > 30$ GeV (dotted) from the $q\overline{q'}$ and qg initial states and the $N\ell$ final state from the qq initial states (solid) at the 8 TeV LHC. The right panel is same as the left panel but at the 14 TeV LHC.

We show in Fig. 4.5 the decomposition of the cross sections shown in Fig. 4.4 for individual final states. The left panel shows the results for $\sqrt{s}$ =8 TeV, while $\sqrt{s}$ =14 TeV results are shown in the right panel. The cross section from the $q\overline{q'}$ initial state dominates over the one from the qg initial state for the cut of $p_T^j > 10$ GeV. With the increase of the p_T^j cut the cross section from the qg initial state becomes dominant for the small mass region of the heavy neutrino, as pointed out in [9]. This is because the parton distribution function (PDF) for gluon is much larger than the PDFs for quarks at the low Bjorken scaling parameter. As the heavy neutrino mass becomes larger, the cross section from $q\overline{q'}$ over takes the one from qg, because the gluon PDF sharply drops toward the high Bjorken scaling parameter.

4.1.2 $N\ell jj$ production processes from $q\overline{q'}$, qg and gg initial states

Next we consider the $N\ell jj$ final state which comes from the $q\overline{q'}$, qg and gg initial states. The relevant Feynman diagrams with the initial $q\overline{q'}$, qg and gg states are shown in Figs. 4.6-4.8. Fig. 4.9 shows the combined heavy neutrino production cross section normalized by the square of the mixing angle from the three initial states. For the final state $N\ell jj$ we impose the minimum transverse momentum for each jet (p_T^j) as 10 GeV, 20 GeV and 30 GeV, respectively. As in the

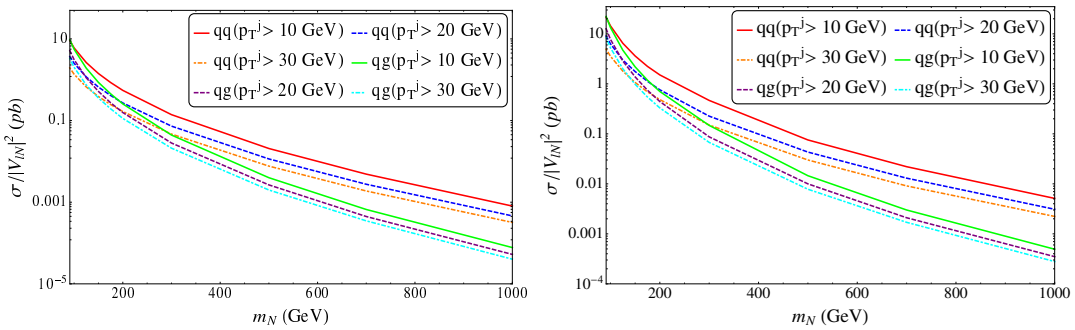

Fig. 4.5. The decomposition of the cross section for the individual initial states for different p_T^j cuts such that $p_T^j > 10$ GeV (solid), $p_T^j > 20$ GeV (dashed) and $p_T^j > 30$ GeV (dot-dashed). The cross sections at the 8 TeV LHC are shown in the left panel where as those at the 14 TeV LHC are shown in the right panel.

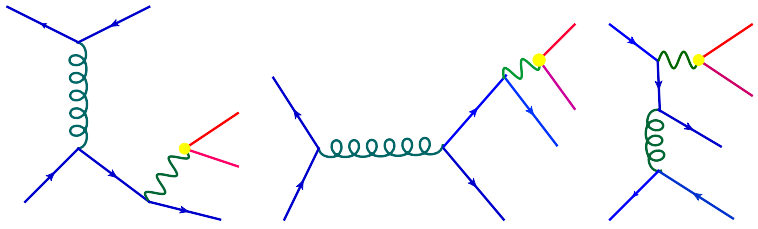

Fig. 4.6. Sample Feynman diagrams for $N\ell jj$ production processes from the $q\overline{q'}$ initial state.

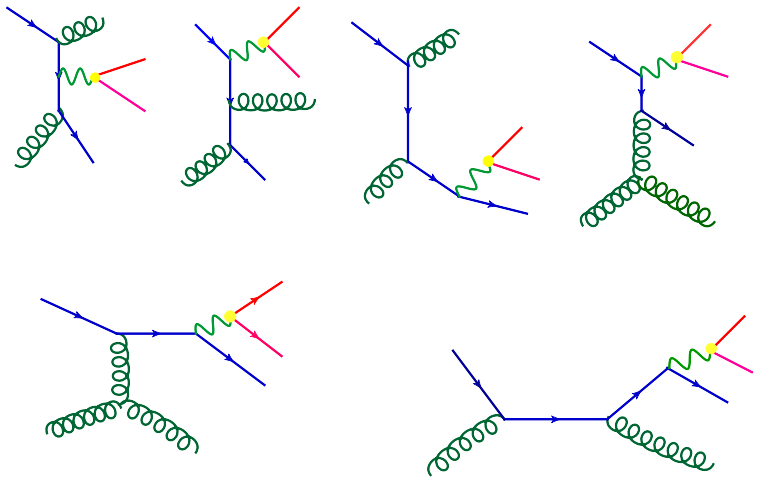

Fig. 4.7. Sample Feynman diagrams for $N\ell jj$ production processes from the qg fusion.

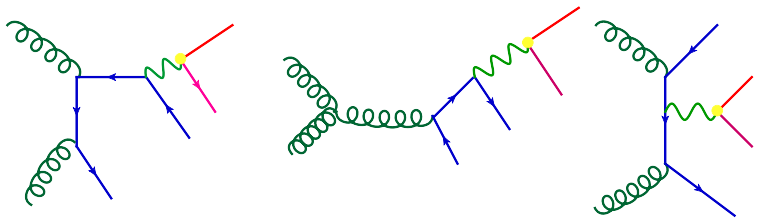

Fig. 4.8. Sample Feynman diagrams for $N\ell jj$ production processes from the gg fusion.

previous sub-section we set the `Xqcut`= p_T^j in MadGraph with the `MLM` matching scheme. The left panel shows the results for $\sqrt{s}$ =8 TeV, while those for $\sqrt{s}$ =14 TeV are shown in the right panel. The $N\ell jj$ cross section dominates over the production cross section for the final state with zero jet for the 10 GeV p_T^j cut, while for a higher p_T^j cut the $N\ell$ cross section dominates.

We show in Fig. 4.10 the decomposition of the cross sections shown in Fig. 4.9 for individual initial states. The left panel shows the results for $\sqrt{s}$ =8 TeV, while results for $\sqrt{s}$ =14 TeV are shown in the right panel. The cross section from the $q\overline{q'}$ initial state dominates over those from the qg and gg initial states for the cut of $p_T^j > 10$ GeV when $m_N \gtrsim 200$ GeV, while for $m_N \lesssim 200$ GeV the qg initial state dominates. This is in contrast with the results for the $N\ell j$, where the $q\overline{q'}$ initial state always dominates the cross section. Although we may think that the gluon fusion channel could dominate, it is found to be always smaller than the other channels. This is because the Bjorken scaling parameters for two gluons can not be small simultaneously in order to produce the heavy neutrino. On the other hand, we expect the gluon fusion channel cross section to become larger as we lower the heavy neutrino mass. We can see in Fig. 4.10 that the gluon fusion channel rises more sharply than the

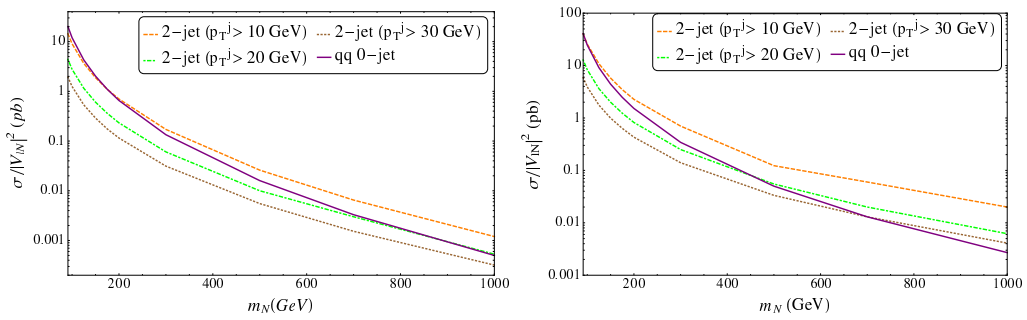

Fig. 4.9. The left panel shows the cross sections as a function of m_N normalized by the square of the mixing angle for the $N\ell jj$ final state for $p_T^j > 10$ GeV (dashed), $p_T^j >$20 GeV (dot-dashed) and $p_T^j > 30$ GeV (dotted) from the $q\overline{q'}$, qg and gg initial states and the $N\ell$ final state from the $q\overline{q'}$ initial state (solid) at the 8 TeV LHC. The right panel shows the results for the 14 TeV LHC.

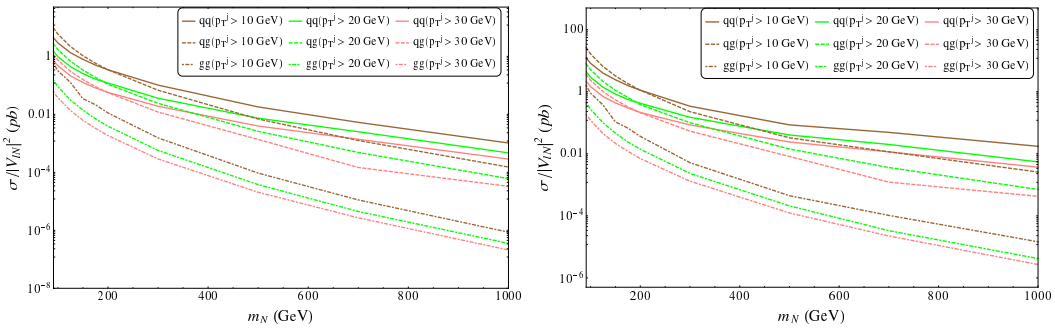

Fig. 4.10. The decomposition of the cross section for the individual initial states for different p_T^j cuts such that $p_T^j > 10$ GeV (solid), $p_T^j > 20$ GeV (dashed) and $p_T^j > 30$ GeV (dot-dashed). The cross sections at the 8 TeV are shown in the left panel where as those at the 14 TeV are shown in the right panel.

others towards the low mass region. We see that as the heavy neutrino mass becomes larger, the cross section from $q\overline{q'}$ over takes those from the qg and gg because the gluon PDF sharply drops towards the high Bjorken scaling parameter.

4.1.3 $N\ell j$ and $N\ell jj$ production processes from photon mediated processes

Apart from the QCD processes we also consider heavy neutrino production at the LHC through the photon mediated processes. There are three types of photon mediated processes. The first one is the elastic process where one photon is radiated from one proton and then scatters with a parton in the other proton. The second one is the inelastic process where one photon is radiated from a parton inside one proton and scatters with a parton inside the other proton (for relevant Feynman diagrams, see Fig. 4.11). The third one is the deep-inelastic scattering mediated by a photon with a large momentum transfer. (See Fig. 4.12 for relevant Feynman diagrams.) Analysis of the deep inelastic process has been performed in [86]. All of these processes have been analyzed in [87] in detail.

We calculate the heavy neutrino production cross sections through the three photon mediated processes. For the deep-inelastic processes we switch off the QCD vertices in `MadGraph`. Our results are shown in Fig. 4.13 for $\sqrt{s} = 14$ TeV LHC. Here we have imposed

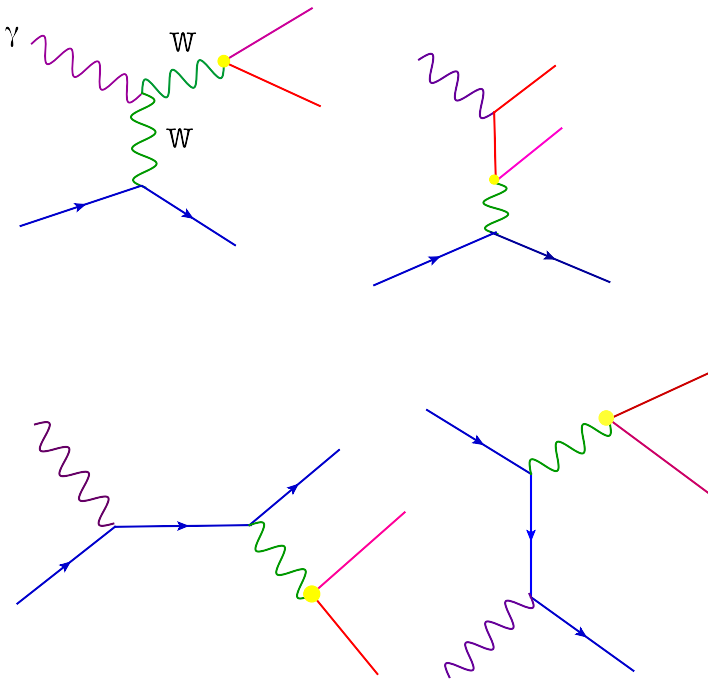

Fig. 4.11. The elastic or inelastic process for the $N\ell j$ final state.

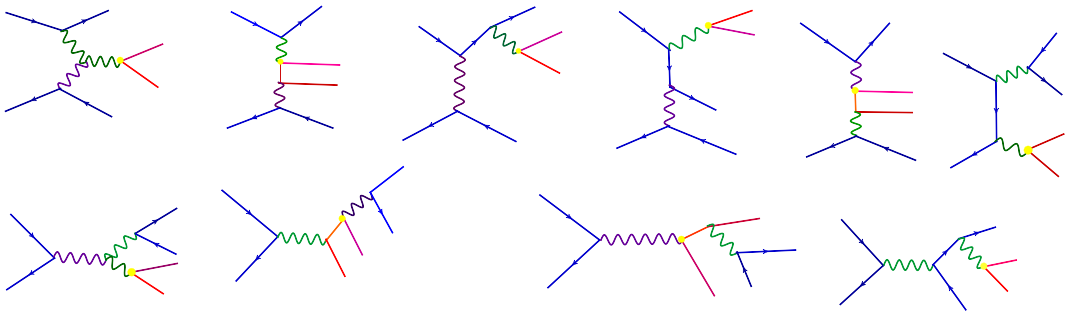

Fig. 4.12. The deep-inelastic processes for the $N\ell jj$ final state mediated by photon.

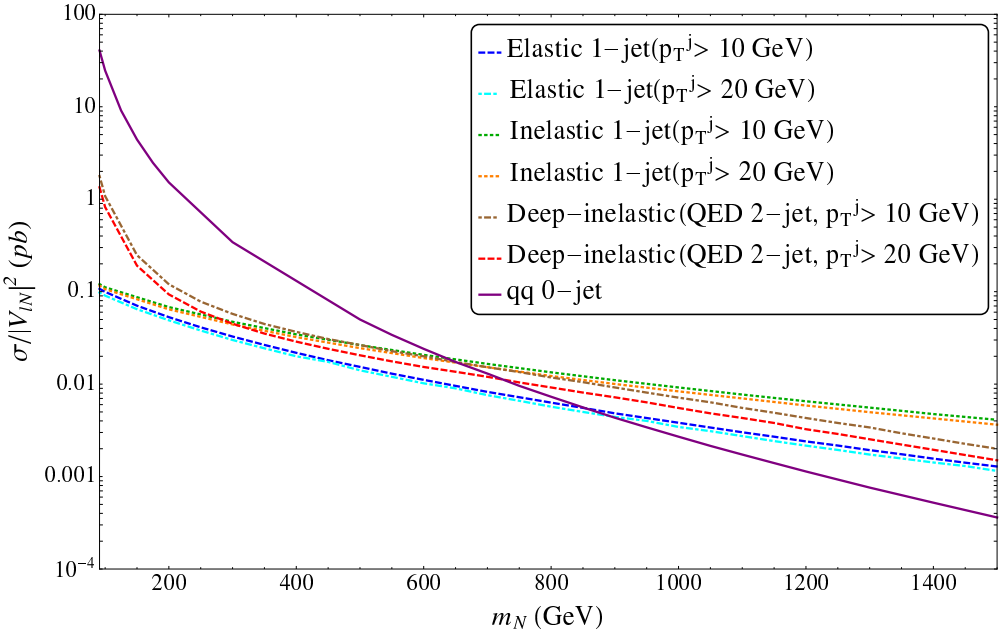

Fig. 4.13. Figure shows the production cross section of the heavy neutrino as a function of m_N and normalized by the square of the mixing angle for the different photon mediated processes at the 14 TeV LHC. The solid line stands for the $N\ell$ final state for the $q\overline{q'}$ initial state. The elastic process for different p_T^j values are shown by the dashed lines. The inelastic processes are represented by the dotted lines. The deep inelastic process (QED 2-jet) is depicted by the dot-dashed lines.

two different values of the p_T^j cuts, $p_T^j > 10$ GeV and 20 GeV. When $m_N \lesssim 400$ (300) GeV, the deep-inelastic process dominates over the other photon mediated processes for $p_T^j > 10$ (20) GeV, and otherwise, the inelastic process dominates. The elastic process is always small compared to the others.

4.2 Data analysis and the upper bounds for the mixing angles

The signal events at the parton level were generated by `MadGraph5`. The showering and hadronization of the events were performed with `PYTHIA6.4` [78] and a fast detector simulation was done using `DELPHES3` [88] bundled with `MadGraph`. Hadrons were clustered into jets using the anti-k_T algorithm as implemented in `FastJet2` [79] with a distance parameter of 0.5. As our signal events are accompanied by n-jets, we incorporate the `MLM` matching prescription according to [80] to avoid the double counting of jets and use the matched cross section and events for the analysis after the detector simulation. We consider two cases for the types of heavy neutrinos. One is the Majorana case for which the signal process is $pp \to N\ell_1^\pm / N\ell_1^\pm j / N\ell_1^\pm jj$, followed by $N \to \ell_2^\pm W^\mp$ and $W^\mp \to jj$. The other is the pseudo-Dirac case for which the signal process is $pp \to N\ell_1^+ / N\ell_1^+ j / Nl_1^+ jj$, followed by

$N \to \ell_2^- W^+$ and $W^+ \to \ell_3^+ \nu$ ($pp \to \overline{N}\ell_1^-/\overline{N}\ell_1^- j/\overline{N}\ell_1^- jj$, followed by $\overline{N} \to \ell_2^+ W^-$ and $W^- \to \ell_3^- \overline{\nu}$).

4.2.1 Same-sign di-lepton plus di-jet signal

For simplicity we consider the case that only one generation of the heavy neutrino is light and accessible to the LHC which couples to only the second generation of the lepton flavor. To generate the events in the `MadGraph` we use the `NN23LO1 PDF` [89] with `Xqcut`= $p_T^j = 20$ GeV and `QCUT`= 25 GeV. We calculate the cross sections for the processes $\sigma_{0-j} = \sigma(pp \to N\mu^\pm \to \mu^\pm\mu^\pm jj)$, $\sigma_{1-j} = \sigma(pp \to N\mu^\pm j \to \mu^\pm j\mu^\pm jj)$ and $\sigma_{2-j} = \sigma(pp \to N\mu^\pm jj \to \mu^\pm jj\mu^\pm jj)$ as functions of m_N. Comparing our generated events with the recent ATLAS results [7] at 8 TeV LHC with a luminosity of 20.3 fb^{-1}, we obtain an upper limit on the mixing angles between the Majorana type heavy neutrino and the SM leptons as a function of m_N. In the ATLAS analysis the upper bound of the production cross section (σ^{ATLAS}) is obtained for the final state with the same-sign di-muon plus di-jet as a function of m_N. Using these cross sections we obtain the upper bounds on the mixing angles as follows

$$|V_{\ell N}|^2_{0-j} \lesssim \frac{\sigma^{ATLAS}}{\sigma_{0-j}}, \tag{4.1}$$

$$|V_{\ell N}|^2_{1-j} \lesssim \frac{\sigma^{ATLAS}}{\sigma_{0-j} + \sigma_{1-j}}, \tag{4.2}$$

and

$$|V_{\ell N}|^2_{2-j} \lesssim \frac{\sigma^{ATLAS}}{\sigma_{0-j} + \sigma_{1-j} + \sigma_{2-j}}. \tag{4.3}$$

Our resultant upper bounds on the mixing angles are shown in Fig. 4.14, along with the bounds from ATLAS [7], CMS [8], LEP (L3) [3], electroweak precision data for electron (EWPD-e) and muon (EWPD-μ) [4] [5] [6], and finally LHC Higgs data (Higgs) [2]. The bound obtained from σ_{0-j} is consistent with the bound presented in [7]. We can see that a significant improvement on the bounds by adding the σ_{1-j} and σ_{2-j} cross sections. We have also calculated the cross sections, σ_{0-j}, σ_{1-j} and σ_{2-j}, for the 14 TeV LHC. Applying the ATLAS bound at 8 TeV with 20.3 fb^{-1} luminosity, we put a prospective upper bound on the mixing angles. We scaled the bound for the luminosities of 300 fb^{-1} and 1000 fb^{-1}. The results are shown in Fig 4.15.

Recently CMS has performed the same-sign di-lepton plus di-jet search [8]. Using this result and adopting the same procedure for the ATLAS result, we calculate the upper bound on the mixing angles at the 8 TeV LHC. The results are shown in Fig. 4.16. A significant improvement for the upper bound on the mixing angle is obtained

by adding the σ_{1-j} and σ_{2-j} results to the σ_{0-j} case. We can see that at the low mass region the bound obtained by the CMS analysis is comparable to our 0-jet plus 1-jet case and in the high mass region that is comparable to our 0-jet case. Using the 8 TeV CMS result [8] we obtain prospective bound at the 14 TeV for the luminosities of 20.3 fb^{-1}, 300 fb^{-1} and 1000 fb^{-1}. The results are shown in Fig. 4.17.

4.2.2 Tri-lepton signal

In this analysis we consider two cases. One is the Flavor Diagonal case (FD), where we introduce three generations of the degenerate heavy neutrinos and each generation couples with a single, corresponding lepton flavor. The other one is the Single Flavor case (SF) where only one heavy neutrino is light and accessible to the LHC. The heavy neutrino couples to only the first or second generation of the lepton flavor. In this analysis we use the `CTEQ6L PDF` [58]. We have calculated the bound on the mixing angle for the tri-lepton case using the $N\ell j$ final state in [9]. In the following we extend this analysis by adding the photon mediated processes to the $N\ell j$ final state. We also include the $N\ell jj$ final state.

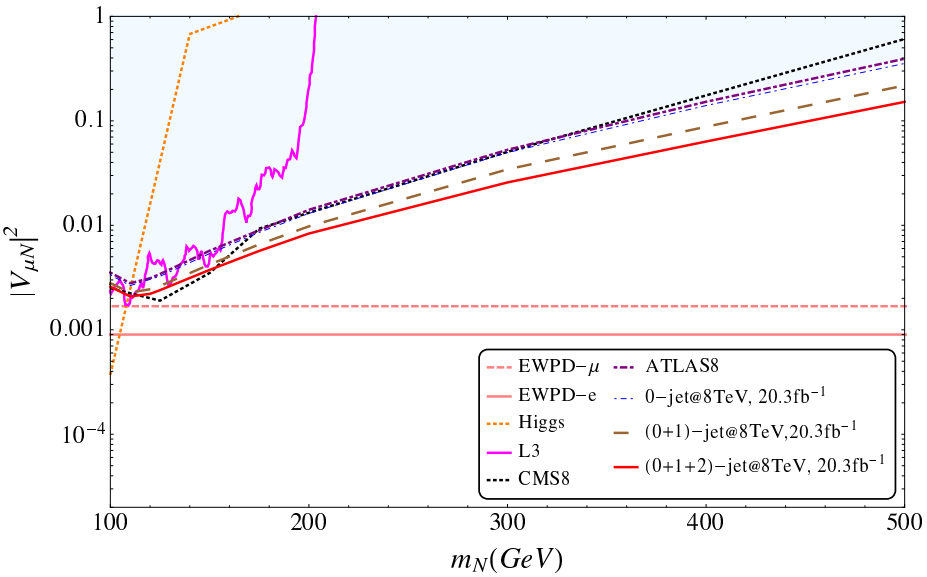

Fig. 4.14. Figure shows the upper bounds of square on the mixing angles as a function of m_N using the ATLAS data at the 8 TeV [7]. The 0-jet (0-jet8, 20.3 fb^{-1}) result is compared with the ATLAS bounds (ATLAS8). The improved results with 1-jet ((dashed), (0+1)-jet@8TeV, 20.3 fb^{-1}) and 2-jet (thick, solid,(0+1+2)-jet@8, 20.3 fb^{-1}) are shown with respect to the bounds obtained by ATLAS [7]. These bounds are compared to (i) the χ^2-fit to the LHC Higgs data [2] (Higgs), (ii) from a direct search at LEP [3](L3), valid only for the electron flavor, (iv) CMS limits from $\sqrt{s}$ =8 TeV LHC data [8] (CMS8), for a heavy Majorana neutrino of the muon flavor and (v) indirect limit from a global fit to the electroweak precision data [4], [5], [6] (EWPD), for both electron (solid, EWPD- e) and muon (dotted, EWPD- μ) flavors. The shaded region is excluded.

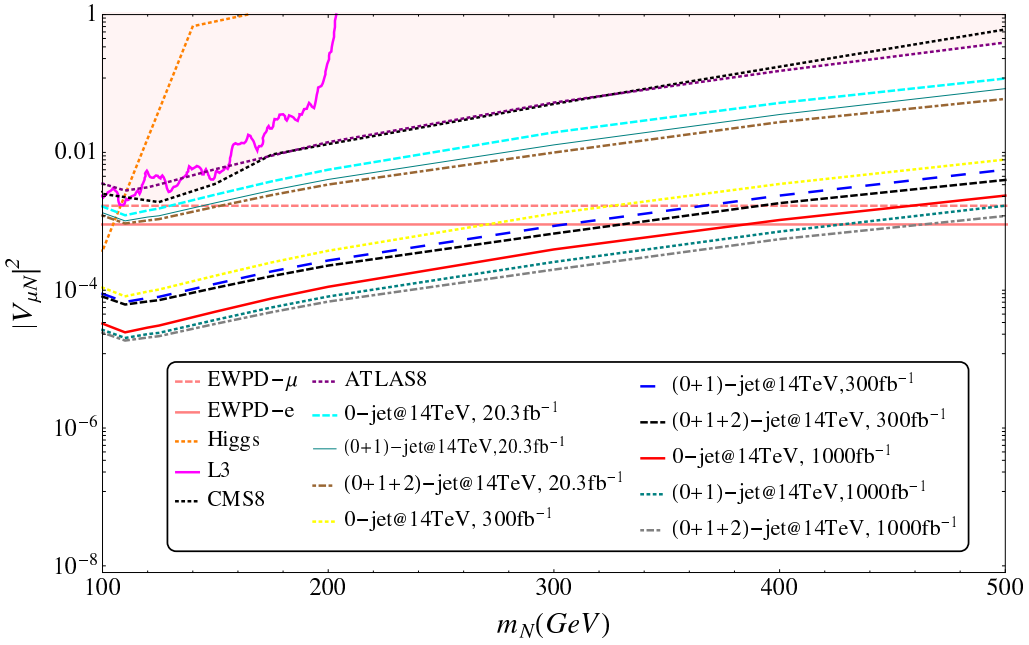

Fig. 4.15. Figure shows the search reach for the square of the mixing angles as a function of m_N at 14 TeV LHC using the ATLAS data at the 8 TeV [7]. In this plot we give a prospective search reach for the 14 TeV. The results with 0-jet (0-jet@14TeV, 20.3 fb^{-1}), 1-jet ((0+1)-jet@14TeV, 20.3 fb^{-1}) and 2-jet ((0+1+2)-jet@14, 20.3 fb^{-1}) are shown at 20.3 fb $^{-1}$. The prospective results with 0-jet(0-jet@14TeV, 300 fb^{-1}), 1-jet ((0+ 1)-jet@14TeV, 300 fb^{-1}) and 2-jet ((0+1+2)-jet@14TeV, 300 fb^{-1}) are also plotted at 300 fb^{-1} luminosity. The prospective results with 0-jet (0-jet@14teV, 1000 fb^{-1}), 1-jet ((0+ 1)-jet@14TeV, 1000fb^{-1}) and 2-jet ((0+1+2)-jet@14TeV, 1000 fb^{-1}) are plotted at 1000 fb^{-1} and compared to (i) the χ^2-fit to the LHC Higgs data [2] (Higgs), (ii) from a direct search at LEP [3](L3), valid only for the electron flavor, (iv) CMS limits from $\sqrt{s}$ =8 TeV LHC data [8] (CMS8), for a heavy Majorana neutrino of the muon flavor and (v) indirect limit from a global fit to the electroweak precision data [4], [5], [6] (EWPD), for both electron (solid, EWPD- e) and muon (dotted, EWPD- μ) flavors. The shaded region is excluded.

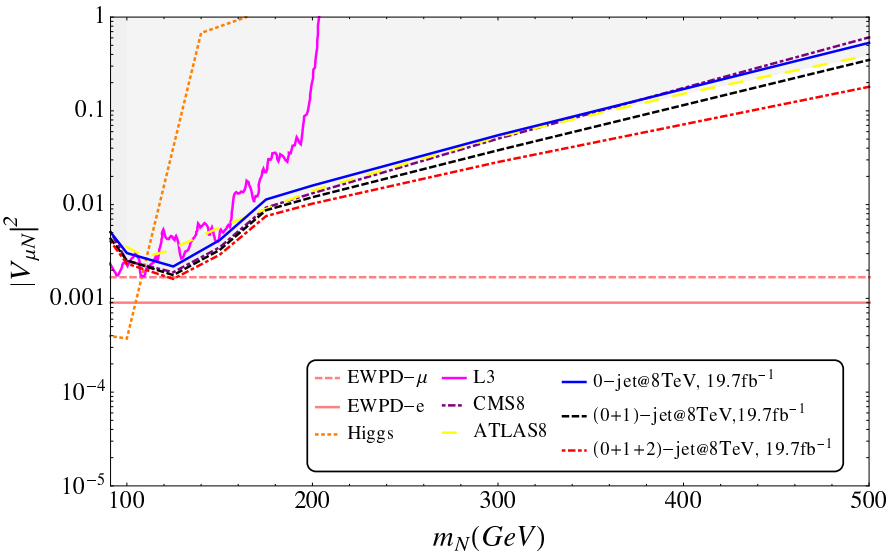

Fig. 4.16. Figure shows the upper bounds on square of the mixing angles as a function of m_N using the CMS data at the 8 TeV [8]. The 0-jet (0-jet@8TeV, 19.7 fb^{-1}) result is compared with the CMS bounds (CMS8). The improved results with 1-jet ((0+ 1)- jet@8TeV, 19.7 fb^{-1}) and 2-jet ((0+ 1+ 2)-jet@8TeV, 19.7 fb^{-1}) are shown with respect to the CMS data from [8]. The bounds are compared to (i) the χ^2-fit to the LHC Higgs data [2] (Higgs), (ii) from a direct search at LEP [3](L3), valid only for the electron flavor, (iv) ATLAS limits from $\sqrt{s}$ =8 TeV LHC data [7] (ATLAS 8), for a heavy Majorana neutrino of the muon flavor and (v) indirect limit from a global fit to the electroweak precision data [4], [5], [6] (EWPD), for both electron (solid, EWPD- e) and muon (dotted, EWPD- μ) flavors. The shaded region is excluded.

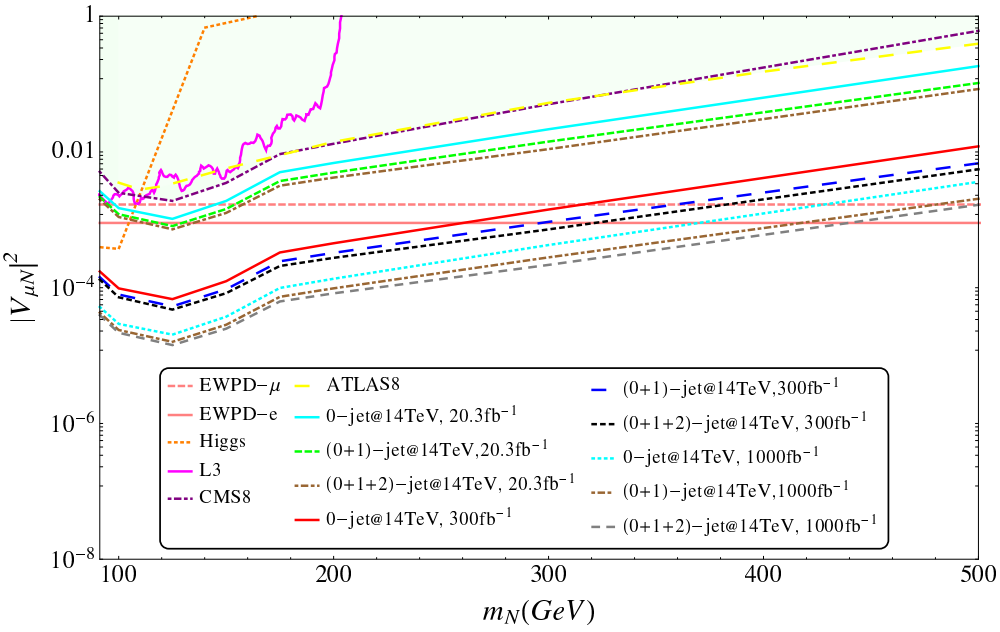

Fig. 4.17. Figure shows the prospective search reach for square of the mixing angles as a function of m_N at the 14 TeV LHC using the CMS data at the 8 TeV [8]. The 0-jet (0-jet@14TeV, 20.3 fb^{-1}), 1-jet ((0+1)-jet@14TeV, 20.3 fb^{-1})and 2-jet ((0+1+2)-jet@14TeV, 20.3 fb^{-1}) are shown at the 20.3 fb^{-1}. The prospective results with 0-jet(0-jet@14TeV, 300 fb^{-1}), 1-jet ((0+ 1)-jet@14TeV, 300 fb^{-1}) and 2-jet ((0+1+2)-jet@14TeV, 300 fb^{-1}) are also plotted at 300 fb^{-1} luminosity. The prospective results with 0-jet (0-jet@14TeV, 1000 fb^{-1}), 1-jet ((0+ 1)-jet@14TeV, 1000fb^{-1}) and 2-jet ((0+1+2)-jet@14TeV, 1000 fb^{-1}) are plotted at 1000 fb^{-1} and compared to (i) the χ^2-fit to the LHC Higgs data [2] (Higgs), (ii) from a direct search at LEP [3](L3), valid only for the electron flavor, (iv) CMS limits from $\sqrt{s}$ =8 TeV LHC data [8] (CMS8), for a heavy Majorana neutrino of the muon flavor and (v) indirect limit from a global fit to the electroweak precision data [4], [5], [6] (EWPD), for both electron (solid, EWPD- e) and muon (dotted, EWPD- μ) flavors. The shaded region is excluded.

We generate the 1-jet and the 2-jet parton level processes separately in `MadGraph` and then gradually hadronize and perform detector simulations with `Xqcut`= p_T^j = 30 GeV and `QCUT`= 36 GeV for the hadronization. In our analysis we use the matched cross section after the detector level analysis. After the signal events are generated, we adopt the following basic criteria, used in the CMS tri-lepton analysis [1]:

(i) The transverse momentum of each lepton: $p_T^\ell > 10$ GeV.

(ii) The transverse momentum of at least one lepton: $p_T^{\ell,\text{leading}} > 20$ GeV.

(iii) The jet transverse momentum: $p_T^j > 30$ GeV.

(iv) The pseudo-rapidity of leptons: $|\eta^\ell| < 2.4$ and of jets: $|\eta^j| < 2.5$.

(v) The lepton-lepton separation: $\Delta R_{\ell\ell} > 0.1$ and the lepton-jet separation: $\Delta R_{\ell j} > 0.3$.

(vi) The invariant mass of each OSSF (opposite-sign same flavor) lepton pair: $m_{\ell^+\ell^-} < 75$ GeV or > 105 GeV to avoid the on-Z region which was excluded from the CMS search. Events with $m_{\ell^+\ell^-} < 12$ GeV are rejected to eliminate background from low-mass Drell-Yan processes and hadronic decays.

(vii) The scalar sum of the jet transverse momenta: $H_T < 200$ GeV.

(viii) The missing transverse energy: $\not{E}_T < 50$ GeV.

The additional tri-lepton contributions come from $N \to Z\nu, h\nu$, followed by the Z, h decays into a pair of OSSF leptons. However, the Z contribution is rejected after the implementation of the invariant mass cut for the OSSF leptons to suppress the SM background and the h contribution is suppressed due to very small Yukawa couplings of electrons and muons. Using different values of $\not{E}_T$ and H_T, the CMS analysis provides different number of observed events and the corresponding SM background expectations. For our analysis the set of cuts listed above are the most efficient ones as implemented by the CMS analysis [1]. To derive the limits on $|V_{\ell N}|^2$, we calculate the signal cross section normalized by the square of the mixing angle as a function of the heavy neutrino mass m_N for both SF and FD cases, by imposing the CMS selection criteria listed above. The corresponding number of signal events passing all the cuts is then compared with the observed number of events at the 19.5 fb^{-1} luminosity [1]. For the selection criteria listed above, the CMS experiment observed:

(a) 510 events with the SM background expectation of 560$\pm$87 events for $m_{\ell^+\ell^-} < 75$ GeV.

(b) 178 events with the SM background expectation of 200±35 events for $m_{\ell^+\ell^-} > 105$ GeV.

In case (a) we have an upper limit of 37 signal events, while in case (b) leads to an upper limit of 13 signal events. Using these limits, we can set an upper bound on $|V_{\ell N}|^2$ for a given value of m_N.

In Fig. 4.18 we plot our results of the upper bound for the SF and FD cases. The thick red dashed line ($SF8_f^{75}$) stands for the results of the SF case by employing the CMS observation (a) whereas the thick red solid line ($SF8_f^{105}$) stands for the results of the SF case by employing the CMS observation (b). The corresponding results for the FD case are represented by the thick blue dashed line ($FD8_f^{75}$) and the thick blue solid line ($FD8_f^{105}$), respectively. The results of the previous analysis [9] are shown by the yellow dashed lines ($SF8_i^{75}$, $SF8_i^{105}$, $FD8_i^{75}$ and $FD8_i^{105}$). Our new results have improved the upper bound on the mixing angles. This improvement becomes more significant in the high m_N region because the photon mediated process dominates the N production cross section (compare Figs. 4.4, 4.9 and 4.13 each other). We have also calculated the cross sections at the 14 TeV LHC. Comparing the cross sections at 14 TeV to those at 8 TeV we have obtained the prospective upper bounds at the 14 TeV LHC, which are shown as the thin solid lines ($SF14_f^{105}$ and $FD14_f^{105}$) above the Z-pole.

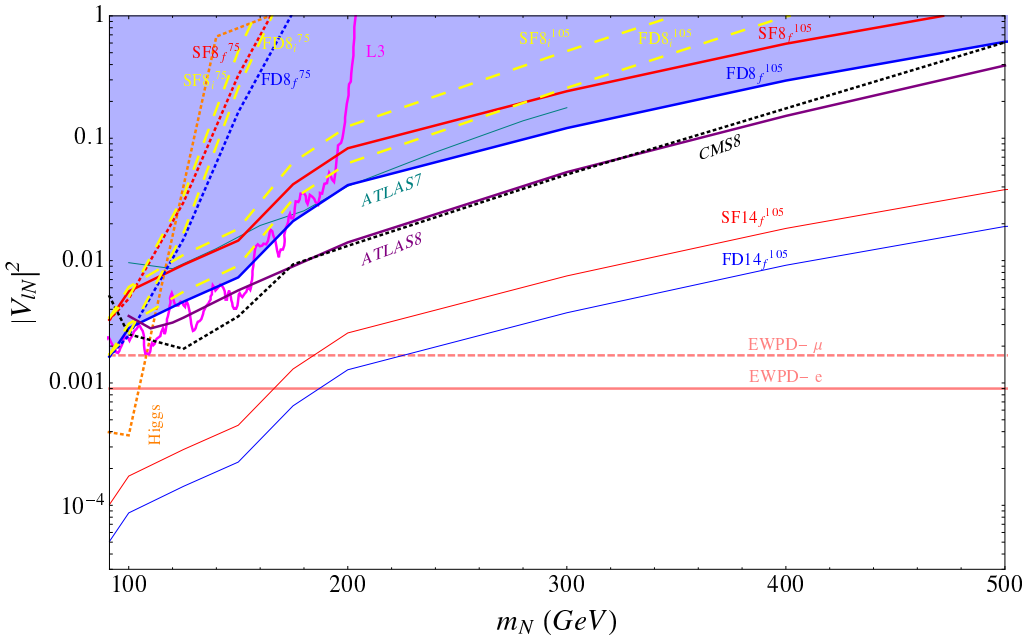

Fig. 4.18. The 95 % CL upper limits on the light-heavy neutrino mixing angles $|V_{\ell N}|^2$ as a function of the heavy Dirac neutrino mass m_N, derived from the CMS tri-lepton data at $\sqrt{s}$ =8 TeV LHC for 19.5 fb^{-1} luminosity [1]. The exclusion (shaded) regions are shown for two benchmark scenarios: (i) single flavor (SF) and (ii) flavor diagonal (FD), with two choices of the selection cut $m_{l^+l^-}$<75 GeV (thick dotted) and >105 GeV (thick solid). The previous results with the selection cut $m_{l^+l^-}$<75 GeV (thick dot-dashed) and >105 GeV (thick large-dashing) at the 1-jet level are shown in this context from [9]. The corresponding conservative projected limits from $\sqrt{s}$ =14 TeV LHC data with 300 fb^{-1} integrated luminosity are shown by thin solid lines ($SF14_f^{105}$ and $FD14_f^{105}$) above the Z-pole. Some relevant existing upper limits (all at 95% CL) are also shown for comparison: (i) from a χ^2-fit to the LHC Higgs data [2] (Higgs), (ii) from a direct search at LEP [3](L3), valid only for the electron flavor, (iii) ATLAS limits from $\sqrt{s}$ =7 TeV LHC data [10] (ATLAS7) and $\sqrt{s}$ =8 TeV LHC data [7] (ATLAS8), valid for a heavy Majorana neutrino of the muon flavor, (iv) CMS limits from $\sqrt{s}$ =8 TeV LHC data [8] (CMS8), for a heavy Majorana neutrino of the muon flavor and (v) indirect limit from a global fit to the electroweak precision data [4], [5], [6] (EWPD), for both electron (solid) and muon (dotted) flavors. The data for 1-jet case from [9] are shown by SF_i^{75}, SF_i^{105}, $FD_i^{75}$and FD_i^{105} (large dashed lines). The shaded region is excluded.

5 CONCLUSION

Apart from the extraordinary agreements between the SM and the experimental observations, the SM has some problems. The neutrinos in SM were considered to be massless, however, the neutrino oscillation experiments have established the existence of small neutrino mass flavor mixing. To explain the tiny neutrino mass we need to the extend the SM with heavy right handed Majorana neutrinos which induce a dimension five operator for the neutrino mass generation, namely, the seesaw mechanism. We also have another possibility to generate the neutrino mass where a small lepton number violating parameter is involved. In this case the smallness of the lepton number violating parameter regulates the tiny neutrino mass. This is called the inverse seesaw mechanism. In this work we have studied the phenomenology of the heavy neutrinos at high energy colliders.

In Chapter 2 we have studied the inverse seesaw scenario and the signature of the pseudo-Dirac heavy neutrino production at the LHC and ILC. In the inverse seesaw scenario, the light neutrino masses are realized by small lepton-number-violating parameters and hence the SM singlet neutrinos have sizable Dirac Yukawa couplings with

the SM lepton doublets and Higgs doublet even for their mass scale being at the TeV scale or smaller. As a result, the heavy neutrinos can be produced at the LHC and ILC. Based on a concrete model realizing the inverse seesaw, we have fixed the model parameters so as to satisfy the experimental results such as the neutrino oscillation data, the precision measurements of the weak boson decays, and the lepton-flavor-violating decays of charged leptons. We have considered two typical cases for the neutrino flavor structures of the model, namely, the FND and FD cases. With the fixed parameters, we have calculated the production cross sections of the heavy neutrinos at the LHC and ILC.

First we have considered simple parameterizations with all zero CP-phases . For the LHC with $\sqrt{s} = 14$ TeV, we have analyzed the productions of the heavy neutrinos with a degenerate 100 GeV mass, providing the tri-lepton final states with the like-sign electrons or muons. After imposing suitable cuts, we have found that the $5-\sigma$ statistical significance of the signal events over the SM background can be achieved for the luminosity around 11 fb^{-1} in the FD case. On the other hand, the production cross sections in the FND case is too small to observe the heavy neutrino signal.

We have also studied the heavy neutrino production at the ILC with $\sqrt{s}$ =500 GeV-1 TeV, where the final state with a single, isolated electron, and di-jet and large missing energy is considered. For the luminosity $\sqrt{s} = 500$ fb^{-1}, we can obtain clear signatures of the heavy neutrinos with mass 150 GeV for the IH mass spectrum in the FND case and the FD case. On the other hand, the significance for the NH mass spectrum in the FND case has been found to be low. Since we can expect the similar efficiencies of the signal and SM background for the final states with different lepton flavors, muon or tau, the heavy neutrinos can be detected with a large statistical significance in the modes for all FND and FD cases.

For completeness, we have also considered the general parameterization for the Dirac neutrino mass matrix by introducing a general orthogonal matrix and CP-phases, for the FND case. In this case, three new parameters, the Dirac CP-phase (δ), the Majorana CP-phase (ρ) and one angle of the orthogonal matrix, are newly involved in our analysis. We have performed a parameter scan and identified the parameter region which satisfies all experimental constraints on the elements of the ϵ-matrix. Then, we have shown the signal cross sections of the heavy neutrino production for the parameters identified. For both of the LHC and ILC cases, we have found significant enhancements of the cross section for the NH case and the resultant

cross section can be of the same order of the FD case. On the other hand, such a remarkable enhancement has not been observed for the IH case.

If the heavy neutrinos are discovered in the future, this indicates that a mechanism of the neutrino mass generation is not due to the conventional seesaw mechanism, because the expected cross section for the conventional seesaw is extremely small. In addition, the flavor dependent signal events from the heavy neutrino productions provide us with valuable information to investigate the flavor structure of the model for the neutrino mass generation.

Finally we comment on the current bound of the heavy neutrino production at the LHC. The ATLAS experiment [82] has reported their results on the search for the heavy neutrinos based on the production through effective four-fermion operators [90]. The vector operator of $(\bar{d}\gamma^\mu u)(\bar{N}\gamma_\mu \ell)/\Lambda^2$ is relevant to our case. The final states with $\ell\ell jj$ ($\ell = e$ or μ) have been analyzed as a signal of the heavy neutrino production, followed by the decay $N \to \ell W$, $W \to jj$. From the data corresponding to an integrated luminosity of 2.1 fb^{-1} at $\sqrt{s} = 7$ TeV, the ATLAS experiment has set the lower bound on the cutoff scale Λ as a function of the heavy neutrino mass ≥ 200 GeV. For example, it is found that $\Lambda \geq 2.8$ TeV for $M = 200$ GeV. We interpret this result to the upper bound on the heavy

neutrino production cross section through the four-fermion operator as $\sigma(q\bar{q}' \to \ell N) \leq 24.0$ fb. In the FD case, we find $\sigma(q\bar{q}' \to \ell N) \simeq 3.77$ fb and therefore, the parameter region we have examined in this paper is consistent with the current LHC results.

In Chapter 3 we have derived the direct collider bounds on electroweak-scale pseudo-Dirac heavy neutrinos, which could be naturally motivated in inverse seesaw models to explain the observed smallness of active neutrino masses by a small lepton number breaking. The derived upper bound on the light-heavy neutrino mixing parameter $|B_{lN}|^2$ is about 2×10^{-3} for $m_N \sim 100$ GeV, and is comparable to the existing best limit from electroweak precision tests. Our analysis provides the first direct limits on the mixing parameter $|B_{lN}|^2$ up to $m_N = 500$ GeV or so. The bounds derived here should be considered as conservative bounds, since optimizing the experimental analysis for our particular trilepton channel, and including the infrared enhancement effects due to t-channel quarks and photons, will yield a much stronger bound. We hope the experimental community will seriously consider this possibility. Finally, the collider bounds could significantly improve with more data from the upcoming LHC run-II with $\sqrt{s} = 13 - 14$ TeV.

In Chapter 4 we have also studied the productions of heavy Majorana and pseudo-Dirac neutrinos from the type-I and the inverse

seesaw mechanisms, respectively. The heavy neutrinos can be produced at the LHC through the sizable mixings with the light neutrinos in the SM. For the heavy neutrino production process, we have considered various initial states such as $q\overline{q'}$, qg and gg as well as photon mediated processes to produce the final states $N\ell$, $N\ell j$ and $N\ell jj$. We have found that the cross section to produce $N\ell j$ from the $q\overline{q'}$ initial state dominates over the qg for $m_N \gtrsim 150$ GeV, while the qg initial state takes over for $m_N \lesssim 150$ GeV at the 8 TeV LHC. This happens because at low Bjorken scaling parameter the gluon PDF dominates over the quark PDF. For the final state $N\ell jj$ the cross section obtained from qg dominates over that from the $q\overline{q'}$ for $m_N \lesssim 200$ GeV, while for $m_N \gtrsim 200$ GeV the $q\overline{q'}$ dominates. The gluon fusion channel follows the cross sections from the qg and $q\overline{q'}$ initial states. The gluon fusion channel can not dominate for the m_N values we studied, because in order to produce the heavy neutrino the Bjorken scaling parameters for the two gluons can not be small simultaneously. We have also studied the photon mediated processes such as elastic, inelastic and the deep-inelastic processes. For $m_N \lesssim 400$ (300) GeV, the deep-inelastic process dominates over the other photon mediated processes for $p_T^j \gtrsim 10$ (20) GeV. The inelastic process dominates over the deep-inelastic process for $m_N \gtrsim 400$

(300) for $p_T^j \gtrsim 10$ (20) GeV. The elastic process always yields the lowest cross section.

We have studied the collider signatures of Majorana and pseudo-Dirac heavy neutrinos. From the Majorana heavy neutrino we consider the same-sign di-lepton plus di-jet in the final state. We have generated the signal cross sections by using `MadGraph`. We compare our results with the recent ATLAS [7] and CMS [8] data at $\sqrt{s} = 8$ TeV with 20.3 fb^{-1} and 19.7 fb^{-1} luminosities, respectively, we have obtained the upper bound on the mixing angles. Using a variety of the initial states we have improved the upper bounds previously obtained in [7] and [8]. For the pseudo-Dirac heavy neutrino we have generated the tri-lepton plus missing energy as the signal events using `MadGraph` and performed the detector simulation for various initial states. Comparing our simulation results with the recent anomalous multi-lepton search results by CMS [1] at $\sqrt{s} = 8$ TeV with 19.5 fb^{-1} luminosity we have obtained the upper bound on the mixing angles, which improves the previously given result in [9]. Finally we have scaled our results at the 8 TeV LHC to obtain a prospective search reach at the 14 TeV LHC with higher luminosities.

REFERENCES

[1] S. Chatrchyan *et al.*, Phys. Rev. **D90**, 032006 (2014), arXiv:1404.5801 [hep-ex] .

[2] P. S. Bhupal Dev, R. Franceschini, and R. N. Mohapatra, Phys. Rev. **D86**, 093010 (2012), arXiv:1207.2756 [hep-ph] .

[3] P. Achard *et al.* (L3), Phys. Lett. **B517**, 67 (2001), arXiv:hep-ex/0107014 [hep-ex] .

[4] J. de Blas, EPJ Web Conf. **60**, 19008 (2013), arXiv:1307.6173 [hep-ph] .

[5] F. del Aguila, J. de Blas, and M. Perez-Victoria, Phys. Rev. **D78**, 013010 (2008), arXiv:0803.4008 [hep-ph] .

[6] E. Akhmedov, A. Kartavtsev, M. Lindner, L. Michaels, and J. Smirnov, JHEP **05**, 081 (2013), arXiv:1302.1872 [hep-ph] .

[7] G. Aad *et al.* (ATLAS), JHEP **07**, 162 (2015), arXiv:1506.06020 [hep-ex] .

[8] V. Khachatryan *et al.* (CMS), Phys. Lett. **B748**, 144 (2015), arXiv:1501.05566 [hep-ex] .

[9] A. Das, P. S. Bhupal Dev, and N. Okada, Phys. Lett. **B735**, 364 (2014), arXiv:1405.0177 [hep-ph] .

[10] S. Chatrchyan *et al.* (CMS), Phys. Lett. **B717**, 109 (2012), arXiv:1207.6079 [hep-ex] .

[11] S. L. Glashow, Nucl. Phys. **22**, 579 (1961).

[12] S. Weinberg, Phys. Rev. Lett. **19**, 1264 (1967).

[13] A. Salam, *Elementary particle theory*, , 367.

[14] C.-N. Yang and R. L. Mills, Phys. Rev. **96**, 191 (1954).

[15] T. Morii, C. S. Lim, and S. N. Mukherjee, *The physics of the standard model and beyond* (2004).

[16] C. P. Burgess and G. D. Moore, *The standard model: A primer* (Cambridge University Press, 2006).

[17] W. N. Cottingham and D. A. Greenwood, *An introduction to the standard model of particle physics* (Cambridge University Press, 2007).

[18] H. Georgi, Front. Phys. **54**, 1 (1982).

[19] P. W. Higgs, Phys. Rev. Lett. **13**, 508 (1964).

[20] P. W. Higgs, Phys. Rev. **145**, 1156 (1966).

[21] F. Englert and R. Brout, Phys. Rev. Lett. **13**, 321 (1964).

[22] G. S. Guralnik, C. R. Hagen, and T. W. B. Kibble, Phys. Rev. Lett. **13**, 585 (1964).

[23] T. W. B. Kibble, Phys. Rev. **155**, 1554 (1967).

[24] G. Aad *et al.* (ATLAS), Phys. Lett. **B716**, 1 (2012), arXiv:1207.7214 [hep-ex] .

[25] S. Chatrchyan *et al.* (CMS), Phys. Lett. **B716**, 30 (2012), arXiv:1207.7235 [hep-ex] .

[26] J. Beringer *et al.* (Particle Data Group), Phys. Rev. **D86**, 010001 (2012).

[27] M. Gell-Mann, Phys. Lett. **8**, 214 (1964).

[28] G. Zweig, CERN-TH-412 , 80 p (1964).

[29] H. Fritzsch, M. Gell-Mann, and H. Leutwyler, Phys. Lett. **B47**, 365 (1973).

[30] N. Cabibbo, *Meeting of the Italian School of Physics and Weak Interactions Bologna, Italy, April 26-28, 1984*, Phys. Rev. Lett. **10**, 531 (1963).

[31] M. Kobayashi and T. Maskawa, Prog. Theor. Phys. **49**, 652 (1973).

[32] B. T. Cleveland, T. Daily, R. Davis, Jr., J. R. Distel, K. Lande, C. K. Lee, P. S. Wildenhain, and J. Ullman, Astrophys. J. **496**, 505 (1998).

[33] J. K. Ahn *et al.* (RENO), Phys. Rev. Lett. **108**, 191802 (2012), arXiv:1204.0626 [hep-ex] .

[34] Y. Abe *et al.* (Double Chooz), Phys. Rev. Lett. **108**, 131801 (2012), arXiv:1112.6353 [hep-ex] .

[35] P. Adamson *et al.* (MINOS), Phys. Rev. Lett. **107**, 181802 (2011), arXiv:1108.0015 [hep-ex] .

[36] F. P. An *et al.* (Daya Bay), Phys. Rev. Lett. **108**, 171803 (2012), arXiv:1203.1669 [hep-ex] .

[37] K. Abe *et al.* (T2K), Phys. Rev. Lett. **107**, 041801 (2011), arXiv:1106.2822 [hep-ex] .

[38] L. E. W. Group (Tevatron Electroweak Working Group, CDF, DELPHI, SLD Electroweak and Heavy Flavour Groups, ALEPH, LEP Electroweak Working Group, SLD, OPAL, D0, L3), (2010), arXiv:1012.2367 [hep-ex] .

[39] S. Schael *et al.* (SLD Electroweak Group, DELPHI, ALEPH, SLD, SLD Heavy Flavour Group, OPAL, LEP Electroweak Working Group, L3), Phys. Rept. **427**, 257 (2006), arXiv:hep-ex/0509008 [hep-ex] .

[40] B. Pontecorvo, Sov. Phys. JETP **7**, 172 (1958), [Zh. Eksp. Teor. Fiz.34,247(1957)].

[41] Z. Maki, M. Nakagawa, and S. Sakata, Prog. Theor. Phys. **28**, 870 (1962).

[42] K. Nakamura *et al.* (Particle Data Group), J. Phys. **G37**, 075021 (2010).

[43] K. Abe *et al.* (T2K), Phys. Rev. Lett. **112**, 181801 (2014), arXiv:1403.1532 [hep-ex] .

[44] F. P. An *et al.* (Daya Bay), Phys. Rev. **D90**, 071101 (2014), arXiv:1406.6468 [hep-ex] .

[45] B.-Z. Hu (Daya Bay), in *Proceedings, 50th Rencontres de Moriond Electroweak interactions and unified theories* (2015) pp. 229–234, arXiv:1505.03641 [hep-ex] .

[46] S.-H. Seo (RENO), *Proceedings of the 15th International Workshop on Neutrino Telescopes (Neutel 2013)*, PoS **Neutel2013**, 018 (2014), arXiv:1312.4111 [physics.ins-det] .

[47] Y. Abe *et al.* (Double Chooz), JHEP **10**, 086 (2014), [Erratum: JHEP02,074(2015)], arXiv:1406.7763 [hep-ex] .

[48] A. Melfo, M. Nemevsek, F. Nesti, G. Senjanovic, and Y. Zhang, Phys. Rev. **D85**, 055018 (2012), arXiv:1108.4416 [hep-ph] .

[49] R. Franceschini, T. Hambye, and A. Strumia, Phys. Rev. **D78**, 033002 (2008), arXiv:0805.1613 [hep-ph] .

[50] P. Minkowski, Phys. Lett. **B67**, 421 (1977).

[51] R. N. Mohapatra and G. Senjanovic, Phys. Rev. Lett. **44**, 912 (1980).

[52] T. Yanagida, Prog. Theor. Phys. **64**, 1103 (1980).

[53] J. Schechter and J. W. F. Valle, Phys. Rev. **D22**, 2227 (1980).

[54] J. A. Casas and A. Ibarra, Nucl. Phys. **B618**, 171 (2001), arXiv:hep-ph/0103065 [hep-ph] .

[55] R. N. Mohapatra, Phys. Rev. Lett. **56**, 561 (1986).

[56] R. N. Mohapatra and J. W. F. Valle, *Proceedings, 23RD International Conference on High Energy Physics, JULY 16-23, 1986, Berkeley, CA*, Phys. Rev. **D34**, 1642 (1986).

[57] I. Gogoladze, N. Okada, and Q. Shafi, Phys. Lett. **B672**, 235 (2009), arXiv:0809.0703 [hep-ph] .

[58] J. Pumplin, D. R. Stump, J. Huston, H. L. Lai, P. M. Nadolsky, and W. K. Tung, JHEP **07**, 012 (2002), arXiv:hep-ph/0201195 [hep-ph] .

[59] S. Antusch, C. Biggio, E. Fernandez-Martinez, M. B. Gavela, and J. Lopez-Pavon, JHEP **10**, 084 (2006), arXiv:hep-ph/0607020 [hep-ph] .

[60] A. Abada, C. Biggio, F. Bonnet, M. B. Gavela, and T. Hambye, JHEP **12**, 061 (2007), arXiv:0707.4058 [hep-ph] .

[61] A. Ibarra, E. Molinaro, and S. T. Petcov, JHEP **09**, 108 (2010), arXiv:1007.2378 [hep-ph] .

[62] A. Ibarra, E. Molinaro, and S. T. Petcov, Phys. Rev. **D84**, 013005 (2011), arXiv:1103.6217 [hep-ph] .

[63] D. N. Dinh, A. Ibarra, E. Molinaro, and S. T. Petcov, JHEP **08**, 125 (2012), [Erratum: JHEP09,023(2013)], arXiv:1205.4671 [hep-ph] .

[64] J. Adam *et al.* (MEG), Phys. Rev. Lett. **107**, 171801 (2011), arXiv:1107.5547 [hep-ex] .

[65] B. Aubert *et al.* (BaBar), Phys. Rev. Lett. **104**, 021802 (2010), arXiv:0908.2381 [hep-ex] .

[66] M. Hirsch, F. Staub, and A. Vicente, Phys. Rev. **D85**, 113013 (2012), [Erratum: Phys. Rev.D91,no.5,059902(2015)], arXiv:1202.1825 [hep-ph] .

[67] A. Abada, D. Das, A. Vicente, and C. Weiland, JHEP **09**, 015 (2012), arXiv:1206.6497 [hep-ph] .

[68] F. del Aguila and J. A. Aguilar-Saavedra, Nucl. Phys. **B813**, 22 (2009), arXiv:0808.2468 [hep-ph] .

[69] F. del Aguila and J. A. Aguilar-Saavedra, Phys. Lett. **B672**, 158 (2009), arXiv:0809.2096 [hep-ph] .

[70] C.-Y. Chen and P. S. B. Dev, Phys. Rev. **D85**, 093018 (2012), arXiv:1112.6419 [hep-ph] .

[71] T. Saito, M. Asano, K. Fujii, N. Haba, S. Matsumoto, T. Nabeshima, Y. Takubo, H. Yamamoto, and K. Yoshioka, Phys. Rev. **D82**, 093004 (2010), arXiv:1008.2257 [hep-ph] .

[72] N. Haba, S. Matsumoto, and K. Yoshioka, Phys. Lett. **B677**, 291 (2009), arXiv:0901.4596 [hep-ph] .

[73] P. S. B. Dev and R. N. Mohapatra, Phys. Rev. **D81**, 013001 (2010), arXiv:0910.3924 [hep-ph] .

[74] A. Das and N. Okada, Phys. Rev. **D88**, 113001 (2013), arXiv:1207.3734 [hep-ph] .

[75] A. Atre, T. Han, S. Pascoli, and B. Zhang, JHEP **05**, 030 (2009), arXiv:0901.3589 [hep-ph] .

[76] J. Lopez-Pavon, S. Pascoli, and C.-f. Wong, Phys. Rev. **D87**, 093007 (2013), arXiv:1209.5342 [hep-ph] .

[77] J. Alwall, M. Herquet, F. Maltoni, O. Mattelaer, and T. Stelzer, JHEP **06**, 128 (2011), arXiv:1106.0522 [hep-ph] .

[78] T. Sjostrand, S. Mrenna, and P. Z. Skands, JHEP **05**, 026 (2006), arXiv:hep-ph/0603175 [hep-ph] .

[79] M. Cacciari, G. P. Salam, and G. Soyez, JHEP **04**, 063 (2008), arXiv:0802.1189 [hep-ph] .

[80] J. Alwall *et al.*, Eur. Phys. J. **C53**, 473 (2008), arXiv:0706.2569 [hep-ph] .

[81] O. Adriani *et al.*, Phys. Lett. **B295**, 371 (1992).

[82] G. Aad *et al.* (ATLAS), Eur. Phys. J. **C72**, 2056 (2012), arXiv:1203.5420 [hep-ex] .

[83] S. Chatrchyan *et al.* (CMS), JHEP **06**, 169 (2012), arXiv:1204.5341 [hep-ex] .

[84] L. Basso, O. Fischer, and J. J. van der Bij, Europhys. Lett. **105**, 11001 (2014), arXiv:1310.2057 [hep-ph] .

[85] S. Antusch and O. Fischer, JHEP **10**, 094 (2014), arXiv:1407.6607 [hep-ph] .

[86] P. S. B. Dev, A. Pilaftsis, and U.-k. Yang, Phys. Rev. Lett. **112**, 081801 (2014), arXiv:1308.2209 [hep-ph] .

[87] D. Alva, T. Han, and R. Ruiz, JHEP **02**, 072 (2015), arXiv:1411.7305 [hep-ph] .

[88] J. de Favereau, C. Delaere, P. Demin, A. Giammanco, V. Lematre, A. Mertens, and M. Selvaggi (DELPHES 3), JHEP **02**, 057 (2014), arXiv:1307.6346 [hep-ex] .

[89] R. D. Ball, V. Bertone, S. Carrazza, L. Del Debbio, S. Forte, A. Guffanti, N. P. Hartland, and J. Rojo (NNPDF), Nucl. Phys. **B877**, 290 (2013), arXiv:1308.0598 [hep-ph] .

[90] F. del Aguila, S. Bar-Shalom, A. Soni, and J. Wudka, Phys. Lett. **B670**, 399 (2009), arXiv:0806.0876 [hep-ph] .